Targeting p130Cas- and microtubule-dependent MYC regulation sensitizes pancreatic cancer to ERK MAPK inhibition

Andrew M. Waters[1], **Tala O. Khatib**[1], **Bjoern Papke**[1], **Craig M. Goodwin**[1], **G. Aaron Hobbs**[1,2], **J. Nathaniel Diehl**[3], **Runying Yang**[1,2], **A. Cole Edwards**[1,4], **Katherine H. Walsh**[5], **Rita Sulahian**[5], **James M. McFarland**[5], **Kevin S. Kapner**[5,13], **Thomas S.K. Gilbert**[2,6], **Clint A. Stalnecker**[1], **Sehrish Javaid**[7], **Anna Barkovskaya**[8], **Kajal R. Grover**[9], **Priya S. Hibshman**[1,4], **Devon R. Blake**[2], **Antje Schaefer**[1,2], **Katherine M. Nowak**[2], **Jennifer E. Klomp**[1], **Tikvah K. Hayes**[3], **Michelle Kassner**[10], **Nanyun Tang**[10], **Olga Tanaseichuk**[11], **Kaisheng Chen**[11], **Yingyao Zhou**[11], **Manpreet Kalkat**[12], **Laura E. Herring**[6], **Lee M. Graves**[1,2], **Linda Z. Penn**[12], **Hongwei H. Yin**[10], **Andrew J. Aguirre**[5,13,14,15], **William C. Hahn**[5,13,14,15], **Adrienne D. Cox**[1,2,7,16], **Channing J. Der**[1,2,3,7,17,*]

[1]Lineberger Comprehensive Cancer Center, University of North Carolina at Chapel Hill, Chapel Hill, NC 27599, USA

[2]Department of Pharmacology, University of North Carolina at Chapel Hill, Chapel Hill, NC 27599, USA

[3]Curriculum in Genetics and Molecular Biology, University of North Carolina at Chapel Hill, Chapel Hill, NC 27599, USA

[4]Department of Cell Biology and Physiology, University of North Carolina at Chapel Hill, Chapel Hill, NC 27599, USA

[5]Broad Institute of MIT and Harvard, Cambridge, MA 02142, USA

*Correspondence: cjder@med.unc.edu.

[6]UNC Michael Hooker Proteomics Center, University of North Carolina at Chapel Hill, Chapel Hill, NC 27599, USA

[7]Oral and Craniofacial Biomedicine PhD Program, School of Dentistry, University of North Carolina at Chapel Hill, Chapel Hill, NC 27599, USA

[8]Institute for Cancer Research, Oslo University Hospital, Oslo 0379, Norway

[9]Department of Nutrition, University of North Carolina at Chapel Hill, Chapel Hill, NC 27599, USA

[10]Cancer and Cell Biology Division, Translational Genomic Research Institute, Phoenix, AZ 85004, USA

[11]Genomics Institute of the Novartis Research Foundation, San Diego, CA 92121, USA

[12]Department of Medical Biophysics, University of Toronto, Toronto, ON M5S, Canada

[13]Department of Medical Oncology, Dana-Farber Cancer Institute, Boston, MA 02215, USA

[14]Harvard Medical School, Boston, MA 02215, USA

[15]Brigham and Women's Hospital, Boston, MA 02215, USA

[16]Department of Radiation Oncology, University of North Carolina at Chapel Hill, Chapel Hill, NC 27599, USA

[17]Lead contact

SUMMARY

To identify therapeutic targets for *KRAS* mutant pancreatic cancer, we conduct a druggable genome small interfering RNA (siRNA) screen and determine that suppression of *BCAR1* sensitizes pancreatic cancer cells to ERK inhibition. Integrative analysis of genome-scale CRISPR-Cas9 screens also identify *BCAR1* as a top synthetic lethal interactor with mutant KRAS. *BCAR1* encodes the SRC substrate p130Cas. We determine that SRC-inhibitor-mediated suppression of p130Cas phosphorylation impairs *MYC* transcription through a DOCK1-RAC1-β-catenin-dependent mechanism. Additionally, genetic suppression of *TUBB3*, encoding the βIII-tubulin subunit of microtubules, or pharmacological inhibition of microtubule function decreases levels of MYC protein in a calpain-dependent manner and potently sensitizes pancreatic cancer cells to ERK inhibition. Accordingly, the combination of a dual SRC/tubulin inhibitor with an ERK inhibitor cooperates to reduce MYC protein and synergistically suppress the growth of *KRAS* mutant pancreatic cancer. Thus, we demonstrate that mechanistically diverse combinations with ERK inhibition suppress MYC to impair pancreatic cancer proliferation.

Graphical Abstract
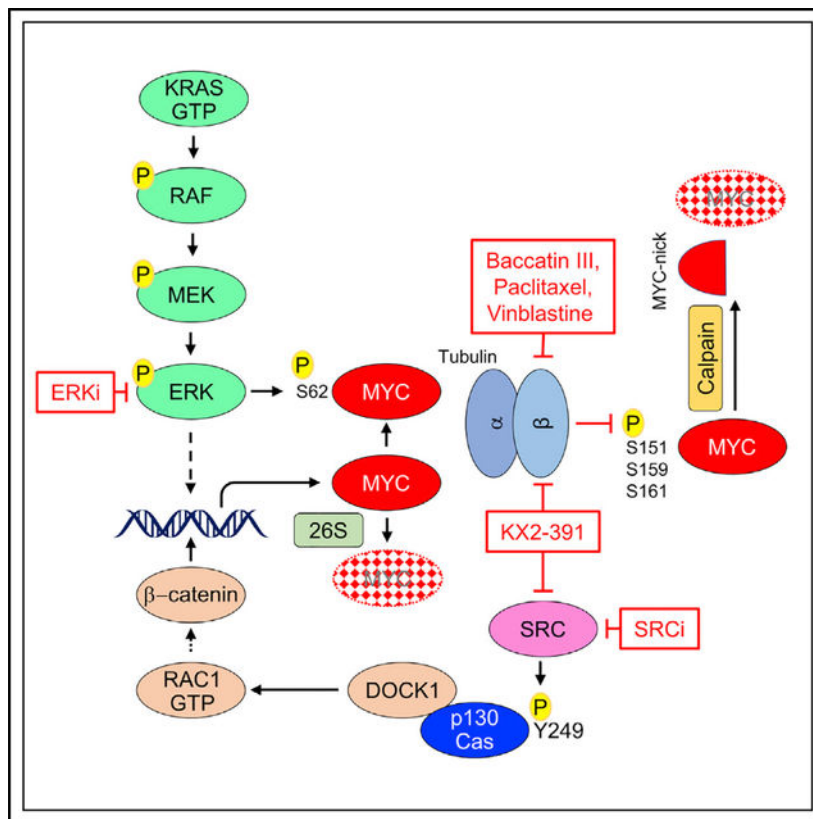
In brief

Using integrated analysis of genome-scale screens, Waters et al. identify *BCAR1* and *TUBB3*, encoding p130Cas and βIII-tubulin, as two pancreatic cancer vulnerabilities that, when inhibited, sensitize *KRAS* mutant PDAC cells to ERK inhibition. Mechanistically, inhibition of p130Cas, βIII-tubulin, and ERK converges on and drives MYC loss to inhibit pancreatic cancer growth.

INTRODUCTION

Activating mutations in *KRAS* are initiating events in pancreatic ductal adenocarcinoma (PDAC) and are required for tumor maintenance (Collins et al., 2012; Ying et al., 2012). Although at least five approaches, spanning over three decades, have been investigated to target KRAS, no clinically evaluated targeted therapies have been approved (Papke and Der, 2017; Ryan and Corcoran, 2018), which has led to the dubious distinction of KRAS being termed "undruggable" (Cox et al., 2014; McCormick, 2015). This is especially disconcerting because the *KRAS* mutation frequency in PDAC is 88%–95% (Prior et al., 2020; Waters and Der, 2018), and pancreatic cancer has the lowest 5-year survival rate (10%) of the major causes of cancer deaths in the United States (Siegel et al., 2020).

Current directions for anti-RAS therapeutic development include direct inhibitors of mutant RAS, inhibitors of RAS effector signaling, and identification of genes whose loss of function is synthetic lethal for mutant RAS (Papke and Der, 2017). While direct inhibitors of one KRAS mutant, G12C, have shown promising activities in early clinical evaluation

(Canon et al., 2019; Hallin et al., 2020), G12C comprises only 1%–2% of KRAS mutations in PDAC (Cox et al., 2014; Waters and Der, 2018). Thus, indirect strategies targeting proteins that critically support the oncogenic driver function of mutant KRAS remain the best approach for PDAC.

Inhibitors of the key KRAS effector signaling network, the RAF-MEK-ERK mitogen-activated protein kinase (MAPK) cascade, have been pursued intensively (Papke and Der, 2017; Waters and Der, 2018). However, RAF inhibitors are plagued by ERK reactivation and promotion of oncogenesis (Hatzivassiliou et al., 2010; Poulikakos et al., 2010; Yen et al., 2018). Inhibitors of MEK have been limited by loss of ERK-dependent feedback inhibition, leading to ERK reactivation and bypass of inhibitor action (Duncan et al., 2012; Little et al., 2011). Furthermore, ERK reactivation drives resistance to KRAS[G12C] inhibitors (Hallin et al., 2020; Ryan et al., 2020; Xue et al., 2020). Addressing these limitations, we showed that inhibitors of the terminal node of the pathway, ERK, can block PDAC tumorigenic growth (Hayes et al., 2016). However, we found that ~50% of *KRAS* mutant PDAC cell lines exhibited *de novo* resistance to ERK inhibition, and ERK inhibitor sensitivity correlated with ERK-inhibitor-mediated loss of the MYC transcription factor, a well-established dependency for KRAS-driven cancer growth (Ozkan-Dagliyan et al., 2020; Soucek et al., 2008; Soucek et al., 2013; Vaseva et al., 2018). Thus, some PDAC cells must regulate MYC in an ERK-independent manner. ERK phosphorylates MYC at residue S62 (pMYC^{S62}) and primes it for GSK3β-mediated phosphorylation at residue T58 (pMYC^{T58}) (Farrell and Sears, 2014). Canonically, phosphatase-mediated loss of pMYC^{S62} then allows FBXW7 E3-ligase-dependent recognition of pMYC^{T58}, leading to MYC degradation. We showed previously that ectopic overexpression of ERK-inhibitor-insensitive phosphodeficient MYC mutants (T58A and/or S62A) rescued ERK1/2 small interfering RNA (siRNA)-mediated loss of MYC and partially rescued ERK-inhibitor-mediated growth suppression in PDAC (Vaseva et al., 2018).

Another indirect therapeutic strategy for targeting RAS proteins is based on synthetic lethality (Huang et al., 2020). However, early genetic loss-of-function screens to identify synthetic lethal genetic interactors with mutant *KRAS* were limited in scope (Cox et al., 2014; Downward, 2015). Recognizing these limitations, ongoing efforts have employed CRISPR-Cas9-based genetic screens that utilize large panels of *KRAS* mutant and wild-type (WT) cancer cell lines (Huang et al., 2020), thus yielding hope for the identification of synthetic lethal targets for *KRAS* mutant cancers (Aguirre et al., 2016; Meyers et al., 2017; Wang et al., 2017).

In the present study, we identified *BCAR1* and *TUBB3* as top sensitizers to ERK inhibition. *BCAR1* encodes the p130Cas signaling scaffold protein, a key substrate for the SRC tyrosine kinase oncoprotein (Barrett et al., 2013; Camacho Leal et al., 2015; Nikonova et al., 2014; Reynolds et al., 2014). *TUBB3* encodes βIII-tubulin, a subunit of microtubules normally only expressed in the brain and testes but overexpressed in PDAC (De Gendt et al., 2011; Lee et al., 2007; McCarroll et al., 2015). Unexpectedly, suppression of either *BCAR1* or *TUBB3* resulted in ERK-independent loss of MYC. Taking advantage of these observations, we determined that combined inhibition of ERK and one or both of two functionally distinct proteins, p130Cas and/or microtubules, caused synergistic loss of MYC

through distinct mechanisms and resulted in apoptotic cell death. Our identification of MYC loss as a mechanistic basis for ERKi-based sensitization, and the efficacy of the triple combination of ERKi + SRC/p130Casi + microtubule inhibition, emphasize the key role of MYC as a therapeutic target and Achilles heel of KRAS in PDAC.

RESULTS

Identification of genes that modulate sensitivity to ERK inhibition

We previously determined that ~50% of *KRAS* mutant PDAC cell lines exhibit *de novo* resistance to ERK inhibitor treatment and that ERKi-mediated MYC loss was a marker of ERK inhibitor sensitivity (Hayes et al., 2016; Vaseva et al., 2018). To determine genetic mechanisms that modulate the sensitivity of *KRAS* mutant PDAC to ERK1/2 inhibition using the ERK1/2-selective inhibitor SCH772984 (ERKi) (Morris et al., 2013), we applied a genetic loss-of-function siRNA screen targeting 6,992 genes of the druggable genome (Figures S1A and S1B; Table S1).

Hits were defined as genes in which at least two siRNAs reduced the ERKi GI_{50} 3-fold compared to control. The 116 genes that met this criterion were enriched for genes encoding proteins that are involved in ERK MAPK signaling (*ARAF*, *MAP2K1*, *DUSP6*, and *DUSP14*; $p = 1.5 \times 10^{-5}$) and in regulation of the cell-cycle G2/M DNA damage checkpoint (*CHK1* and *AURKA*; $p = 3.4 \times 10^{-5}$) (Figures S1C) (Krämer et al., 2014; Szklarczyk et al., 2015). We did not identify any desensitizers to ERK inhibitor treatment, nor did any hits enhance the growth of *KRAS* mutant PDAC cells under vehicle treatment. The top 38 of the 116 hits shifted the GI_{50} 5-fold relative to controls in both biological replicates or 10-fold in at least one replicate (Figure 1A). Of these 38 genes, which encode proteins with highly diverse functions (Table S2), we pursued *BCAR1* and *TUBB3* for further analysis.

Identification of *BCAR1* as a synthetic lethal interactor in *KRAS* mutant PDAC

To identify synthetic lethal interactions with oncogenic *KRAS* mutants, we analyzed genome-scale CRISPR-Cas9 loss-of-function screens from over 500 cancer cell lines from the Cancer Dependency Map (https://www.depmap.org/). We identified preferential genetic dependencies in *KRAS* mutant versus *KRAS*-WT cancer cell lines (Figure 1B). As expected, knockout of *KRAS* was the most significant preferential dependency between *KRAS* mutant and WT cancer cell lines. Two additional hits, *RAF1* and *FOSL1*, are well-validated dependencies for KRAS-driven cancer growth (Blasco et al., 2011; Karreth et al., 2011; Vallejo et al., 2017; Wang et al., 2017). Loss of *BCAR1*, also identified in our ERKi sensitivity screen (Figure 1A), was among the top synthetic lethal interactors with mutant *KRAS*. Finally, we compared CRISPR-Cas9 dependencies in *KRAS*-dependent PDAC cancer cell lines with those observed in *KRAS*-independent cancer cell lines of all lineages. We identified *BCAR1* among the most preferential dependencies in *KRAS*-dependent PDAC cell lines (Figure 1C), indicating that PDAC may be especially vulnerable to *BCAR1* suppression. We determined *BCAR1* appears to be synthetic lethal specifically for *KRAS* mutant pancreatic cancer, and no clear trend emerges for most of the other cancer types, including other cancer types with *RAS* mutation frequencies (Figure S1D). Integrated analyses of these data and the ERKi sensitization data suggested a mechanistic role in which

BCAR1 may be a synthetic lethal target of *KRAS* mutant PDAC because of its role in sensitizing PDAC cells to ERK inhibition.

To understand how *BCAR1* dependency may relate to other genetic dependencies, we performed a Pearson correlation analysis of *BCAR1* dependency with all other gene dependencies across the Cancer Dependency Map dataset (Figure 1D). We observed that 14 of the top 25 genetic dependencies most correlated with *BCAR1* dependency in CRISPR-Cas9 screening data had previously been associated with *BCAR1*, including *SRC* and *RAC1*. These observations further support a crucial role for p130Cas in coordinating essential tumorigenic signaling processes.

p130Cas suppression reduces MYC and inhibits proliferation in a subset of PDAC cell lines

p130Cas, the protein product of *BCAR1*, is a critical scaffold/adaptor protein implicated in spatiotemporal regulation of focal adhesion turnover, migration, cell-cycle progression, invasion, and mechanotransduction (Barrett et al., 2013; Camacho Leal et al., 2015; Nikonova et al., 2014; Reynolds et al., 2014). Moreover, *BCAR1* has been identified twice as a susceptibility locus for pancreatic cancer in genome-wide association studies (Childs et al., 2015; Wolpin et al., 2014), and overexpression of *BCAR1* has been identified as a marker for pancreatic cancer in a transcriptome-wide association study (Zhong et al., 2020). Concordantly, we observed KRAS-driven transformation of hTERT-immortalized human pancreatic cells (HPNE-RAS) was associated with increased p130Cas protein, and *KRAS* mutant PDAC cell lines expressed more p130Cas than untransformed HPNE-DT cells (Figure S1E).

We then determined the consequences of *BCAR1* suppression on the proliferation of a panel of *KRAS* mutant PDAC cell lines. siRNA-mediated *BCAR1* suppression (siBCAR1), as measured by loss of p130Cas expression (Figure 2A), was sufficient to reduce proliferation and clonogenic growth in three of the nine *KRAS* mutant PDAC cell lines (Figures 2B and S2A). Since we previously found that loss of MYC was a key marker of ERKi sensitivity (Hayes et al., 2016), we examined whether *BCAR1* suppression, like ERKi, decreased MYC protein levels. We found that *BCAR1* suppression caused a reduction in MYC protein in the three cell lines that were growth inhibited (Figure 2A). We previously determined that MYC was essential for PDAC growth *in vitro* and *in vivo* (Vaseva et al., 2018). To determine whether MYC loss was contributing to the growth inhibition in Pa16C cells, we genetically suppressed *BCAR1* and overexpressed hemagglutinin (HA)-tagged MYC from a heterologous promoter (Figure 2C). Restoring MYC levels partially rescued the proliferative defect upon *BCAR1* genetic suppression, indicating siBCAR1-dependent loss of MYC is partially responsible for the growth defect (Figure 2D).

To determine the consequences of *BCAR1* suppression on the activity/expression of the kinome, we applied multiplexed kinase inhibitor bead/mass spectrometry (MIB/MS) analyses (Duncan et al., 2012) to Pa16C cells treated with siBCAR1 (Figure S2B). One downregulated kinase was CDK9, a regulator of *MYC* gene transcription (Blake et al., 2019). We also found that *BCAR1* suppression downregulated the critical G1 cell-cycle regulators CDK4 and CDK6, suggesting one mechanism of siBCAR1-treatment-induced growth suppression may be CDK4/6-mediated G1 arrest. We next determined that *BCAR1*

suppression resulted in hypophosphorylation and activation of the CDK4/6 substrate, the RB tumor suppressor protein (Figure S2C), and in G1 cell-cycle arrest (Figure S2D). Thus, these analyses identified an unanticipated role for p130Cas in proliferation via regulation of CDK4/6 activity/expression and RB inactivation.

To evaluate whether *BCAR1* suppression also inhibited growth through promoting apoptosis, we stably infected PDAC cells with small hairpin RNAs (shRNAs) targeting *BCAR1.* Stable suppression of p130Cas expression was associated with reductions in MYC protein, proliferation, clonogenic growth, and increased apoptosis (Figures S3A–S3C). In PANC-1 cells, we observed reductions in MYC protein and proliferation upon shRNA-mediated, but not siRNA-mediated, suppression of *BCAR1*, indicating temporal *BCAR1*-mediated MYC regulation. We conclude that p130Cas-dependent growth is mediated, in part, by maintaining MYC protein levels.

p130Cas suppression sensitizes PDAC cells to ERK inhibition by increasing apoptosis in a MYC-dependent manner

Our MIB/MS results showed that siRNA suppression of *BCAR1* significantly dysregulated MAPK signaling (*MAP2K1*, *MAP2K3*, *IGF1R*, *EGFR*, *MAP3K4*, *INSR*, *TAOK1*, *EPHA2*, and *PRKACB*; p = 7.36×10^{-7}), suggesting that MAPK signaling may compensate for *BCAR1* loss (Figure S2B). This could contribute to the basis for our identification of *BCAR1* in an ERKi sensitization screen.

As we described previously (Hayes et al., 2016; Vaseva et al., 2018), the dose-dependent reduction in phosphorylated ERK (pERK) upon ERKi treatment correlated with loss of phosphorylation of two key ERK substrates, MYC at S62 and RSK at T359/S363 (Figure S3D). This was associated with an increased level of the cyclin-dependent kinase inhibitor protein and G1 cell-cycle marker p27 KIP1 and a significant G1 cell-cycle arrest (Figure S3E), but not a substantial increase in apoptotic cells (Figure S3F). Therefore, ERKi treatment causes cytostatic rather than cytotoxic growth suppression.

We next determined if *BCAR1* suppression enhanced sensitivity to ERKi treatment in a panel of PDAC lines. We found that with siBCAR1 treatment, the GI_{50} for ERKi treatment was reduced in five of seven PDAC cell lines evaluated (Figure S4A). Similarly, cells stably infected with shRNA targeting *BCAR1* (shBCAR1) were growth inhibited and underwent significant further growth reduction that was enhanced with ERKi (Figure S4B). The enhanced growth suppression was due to increased apoptosis, with *BCAR1* suppression alone promoting apoptosis that was enhanced synergistically by co-treatment with ERKi in three of five cell lines (Figure 2E), as indicated by combination indexes <1 using the Bliss independence model (Foucquier and Guedj, 2015). To verify the on-target activity of SCH772984, we determined that a chemically and mechanistically distinct ERK1/2-selective inhibitor, ulixertinib/BVD-523, caused synergistic and apoptotic growth suppression when combined with *BCAR1* genetic suppression (Figure S4C).

Because either ERKi treatment or *BCAR1* suppression alone can reduce MYC levels, we determined if loss of MYC may contribute to the enhanced growth suppression seen upon concurrent treatment with ERKi and *BCAR1* silencing. Whereas either ERKi treatment or

BCAR1 silencing alone reduced MYC in four of five PDAC cell lines (Figure 2F), concurrent ERKi and *BCAR1* genetic suppression further reduced MYC in all the cell lines. Likewise, ulixertinib caused MYC loss that was potentiated with *BCAR1* genetic suppression (Figure S4D). These results suggest *BCAR1* genetic suppression and ERK inhibition cooperate to impair PDAC growth through loss of MYC.

To determine the basis for *BCAR1*-suppression-induced loss of MYC protein, we performed qRT-PCR on Pa16C cells treated with shBCAR1 and observed a >2.5-fold decrease in *MYC* transcription that was not reduced further upon ERKi treatment (Figure S4E). We showed previously that ERK inhibition causes loss of MYC primarily through increased MYC protein degradation and, to a lesser degree, through suppression of *MYC* transcription (Vaseva et al., 2018). Treatment with the proteasome inhibitor MG132 did not prevent the loss of MYC protein observed upon suppression of *BCAR1* (Figure S4F). Furthermore, MYC protein half-life was unchanged upon *BCAR1* suppression (Figure S4G). These observations indicate that concurrent suppression of p130Cas expression and ERK activity enhances loss of MYC through complementary mechanisms of decreasing gene transcription and protein stability, respectively.

We then further investigated the mechanism behind the synergistic apoptosis induced by concurrent suppression of ERK and p130Cas. We found that while ERKi treatment dose-dependently reduced MYC in both *BCAR1*-suppressed and control cells as expected, the reduction was more substantial upon concurrent suppression of *BCAR1* (Figure 2G). Inversely correlated with MYC levels, ERKi caused a modest dose-dependent increase in PARP cleavage and apoptosis that was enhanced in shBCAR1-treated cells (Figures 2G and 2H). These data support a mechanism whereby concurrent suppression of ERK and p130Cas function more effectively reduces MYC levels and results in a shift from cytostatic to cytotoxic impairment of PDAC growth.

SRC inhibition transcriptionally reduces MYC and synergizes with ERKi in a subset of PDAC cell lines

Phosphorylation of p130Cas by SRC creates recognition sites for SH2-domain-containing proteins. Loss of *SRC* was also identified in our correlation analysis as a genetic signature that mimicked loss of *BCAR1* (Figure 1D). Therefore, we determined if pharmacologic inhibition of SRC would impair p130Cas function and cause loss of MYC. Treatment of Pa16C and Pa02C cell lines with the SRC inhibitor saracatinib (SRCi) caused a dose-dependent reduction in p130Cas phosphorylation (pp130Cas) at Y249, a major SRC phosphorylation site, and concurrent loss of MYC protein (Figure 3A). The loss of MYC in Pa02C cells upon SRCi treatment was not expected, because shBCAR1 treatment increased rather than decreased MYC (Figure 2F). Resolving this apparent discrepancy, we found that although shBCAR1 treatment suppressed total p130Cas in both lines, it conversely increased pp130Cas in Pa02C cells (Figure 3B). Thus, we found a strong correlation between the levels of MYC protein and phosphorylated rather than total p130Cas.

We further evaluated whether SRCi can serve as a pharmacologic inhibitor of p130Cas and phenocopy genetic suppression of *BCAR1*. As we observed upon si/shBCAR1-mediated suppression of total p130Cas protein levels, SRCi-treatment-induced reduction in MYC was

also associated with a reduction in *MYC* transcription and G1 cell-cycle arrest (Figures 3C and S5A). Similar to what we observed upon *BCAR1* genetic suppression, SRCi-induced MYC loss was incompletely rescued by MG132 treatment (Figure S5B), and MYC protein half-life was not reduced (Figure S5C). These results indicate that the major mechanism by which SRCi regulates MYC is transcriptional and that SRCi phenocopies p130Cas suppression. Additionally, similar to combining genetic suppression of *BCAR1* with ERKi, concurrent SRCi and ERKi treatment caused synergistic growth suppression (Figure S5D) that was associated with synergistic suppression of MYC (Figure 3D) and increased apoptosis (Figures 3E and 3F). Increased apoptosis was also seen with SRCi in combination with ulixertinib, supporting on-targeting activity of SCH772984 (Figure S5E). These data support the use of SRCi as a pharmacologic inhibitor of p130Cas-dependent regulation of MYC.

To establish a mechanism for p130Cas-dependent regulation of MYC levels, we determined whether genetic suppression of known p130Cas-associated proteins phenocopies genetic suppression of p130Cas and causes loss of MYC protein. We found that shRNA suppression of *DOCK1*, *ZNF384*, *PIK3CA* (encodes PI3K p110α), or *BCAR3* (a hit in the ERKi sensitizer screen; Figure 1A) caused loss of MYC (Figure 3G). Knockdown of *ZNF384*, *BCAR3*, or *PIK3CA* also reduced phosphorylated p130Cas, indicating the encoded proteins may regulate MYC indirectly through regulation of p130Cas phosphorylation. In contrast, genetic suppression of *DOCK1* reduced MYC without a concomitant reduction in pp130Cas. Therefore, we speculated that DOCK1 (DOCK180), which associates with p130Cas upon phosphorylation by SRC (Smith et al., 2008), may regulate MYC by acting downstream of pp130Cas. Specifically, we propose a pathway whereby DOCK1 can regulate MYC expression through the small GTPase RAC1 and the transcription factor β-catenin. DOCK1 is a guanine nucleotide exchange factor and activator of RAC1 (Kiyokawa et al., 1998). RAC1 activation enhances nuclear accumulation of β-catenin (Wu et al., 2008). β-Catenin binds to the *MYC* promoter and its 3′ enhancer to stimulate *MYC* gene expression (He et al., 1998; Yochum et al., 2008). In agreement, we found nuclear-localized activated β-catenin (S33A/S37A/T41A/S45A, "4A") (Figure S5F) increased MYC protein (Figure S5G) and transcriptional activity (Figure S5H). Additionally, we determined from our correlation analysis that *RAC1* loss has a genetic signature like *BCAR1* loss (Figure 1D). Furthermore, like *BCAR1*, we identified *CTNNB1*, the gene that encodes β-catenin, as a genetic dependency in *KRAS* mutant cancers (Figure 1B).

Consistent with an association between p130Cas and DOCK1-RAC1 signaling, we found that shBCAR1 treatment of Pa16C cells decreased activated RAC1-GTP (Figure S6A). Moreover, we found this led to a reduction in active-β-catenin. We next determined that shRNA-mediated suppression of *DOCK1* or *RAC1* phenocopied shBCAR1-associated alterations in cell morphology (Figure S6B). Further, shDOCK1 and shRAC1 treatment also caused loss of MYC that was restored by overexpressing activated β-catenin (Figure S6C). Importantly, shDOCK1 and shRAC1 treatment resulted in clonogenic and proliferative defects that could be partially rescued by overexpressing activated β-catenin (Figures S6D and S6E). Taken together, these data support a mechanism whereby SRC-dependent phosphorylation of p130Cas regulates *MYC* transcription through a DOCK1-RAC1-β-catenin pathway.

Microtubule inhibition degrades MYC protein half-life in a calpain-dependent manner and synergizes with ERKi in PDAC cell lines

We next evaluated a second hit from our screen. *TUBB3*, encoding βIII-tubulin, was one of the 38 strongest ERKi sensitizers (Figure 1A), and the related gene *TUBB6* was among our top 116 hits (Figure S1C). β-Tubulin and α-tubulin form heterodimers that comprise microtubules, and their dynamic assembly/disassembly are essential for proper mitotic spindle function and completion of mitosis (Jouhilahti et al., 2008). One reason we pursued the evaluation of βIII-tubulin was because G2/M DNA damage checkpoint regulation was the most dysregulated pathway in our screen (p = 3.4×10^{-5}). Additionally, βIII-tubulin overexpression in pancreatic cancer has been described and shown to promote growth and resistance to chemotherapy (Lee et al., 2007; McCarroll et al., 2015).

βIII-Tubulin is normally expressed in terminally differentiated neurons and in the testes (De Gendt et al., 2011). However, in agreement with a prior study that identified *TUBB3* overexpression in pancreatic cancer and a correlation between βIII-tubulin expression and KRAS activation (Lee et al., 2007), we detected high levels of βIII-tubulin in six of eight *KRAS* mutant PDAC cell lines, and we found an increase in βIII-tubulin protein upon *KRAS* mutant transformation of HPNE-DT cells (Figures 4A and S7A). Using siRNAs targeting *TUBB3*, we observed growth inhibition in all PDAC lines tested (Figure S7B), in agreement with previous studies that found *TUBB3* suppression caused a proliferative defect in pancreatic cancer cells (Lee et al., 2007; McCarroll et al., 2015). Unexpectedly, we again found that growth inhibition was associated with loss of MYC (Figure S7C), as well as with an increase in phospho-histone H3 S10 (pHistone H3), a marker of mitotic arrest (Figure S7D). Finally, *TUBB3* depletion increased apoptosis (Figure S7E).

We next utilized pharmacologic inhibitors to block β-tubulin function. The taxanes baccatin III and paclitaxel bind to β-tubulin, enhancing microtubule stability and disrupting microtubule dynamics, causing G2/M arrest and apoptosis (Perez, 2009). As expected, baccatin III and paclitaxel caused a dose-dependent increase in microtubules (Figure S7F) and pHistone H3 (Figures 4B and 4C), as well as G2/M arrest (Figure S7G) and apoptosis (Figure 4D). Similarly, we found that treatment with vinblastine, which binds to β-tubulin and destabilizes microtubules (Figure S7H), increased pHistone H3, G2/M arrest, and apoptosis (Figures S7I–S7K).

As observed previously with paclitaxel treatment (Dai et al., 2001; MacKeigan et al., 2000; McDaid and Horwitz, 2001; Okano and Rustgi, 2001; Orr et al., 2003; Schmid-Alliana et al., 1998; Shinohara-Gotoh et al., 1991), we found that paclitaxel, baccatin III, and vinblastine all caused a dose-dependent increase in pERK (Figures 4B, 4C, and S7I). Although a previous study found that MEK inhibition blocked paclitaxel-induced activation of ERK (MacKeigan et al., 2000), suggesting that this activation was due to increased upstream signaling, we observed no increase in phosphorylated MEK (pMEK). Instead, we observed downregulation of the ERK phosphatases DUSP4 and DUSP6 (Figure 4C), suggesting that paclitaxel activation of ERK is mediated by loss of negative regulation.

Our previous work showed ERK activity promotes MYC protein stability in PDAC cells (Vaseva et al., 2018); therefore, we were surprised to see that β-tubulin inhibitor treatment

increased ERK activation and yet concomitantly decreased MYC protein (Figures 4B, 4C, and S7I). Because loss of MYC has not been described previously as a consequence of β-tubulin inhibitors, we next investigated a mechanism for loss of MYC. Paclitaxel and baccatin III stimulated a limited increase in *MYC* transcription that was abrogated upon concurrent ERK inhibitor treatment (Figure S8A). Conversely, we determined that paclitaxel and baccatin III caused a >2-fold reduction in MYC protein half-life (Figure 4E), indicating that the overall reduction in MYC levels induced by β-tubulin inhibitor treatment is driven by a reduction in protein stability.

To determine the mechanism by which microtubule inhibitors shortened MYC protein half-life, we speculated that this activity may involve phosphorylation-regulated protein modification. To address this possibility, we generated a panel of 10 phospho- or lysine-deficient HA-tagged MYC mutants based on MYC modifications we identified previously (Dingar et al., 2018) (Table S3). We established PDAC cells stably expressing WT MYC, MYC^{T58A}, MYC^{S62A}, and the 10 different MYC mutants. After confirming WT- and mutant-MYC expressing cells expressed comparable levels of MYC protein (Figure S8B), we determined that MYC mutant 5 (S151/159/161A) was resistant to paclitaxel-mediated MYC degradation (Figure S8C). Notably, we observed a ~33-kDa degradation species in the WT-MYC-overexpressing cells that we did not observe in the Mut-5-MYC-overexpressing cells (Figure S8C).

We speculated that the 33-kDa MYC fragment may correspond to a previously described "MYC-nick" fragment that binds to and stabilizes microtubules (Conacci-Sorrell et al., 2010). To address this possibility, we determined if the 33-kDa fragment shared properties with MYC-nick. MYC-nick is formed through calpain-dependent cleavage at amino acid 298, generating a MYC-nick fragment that can be inhibited by using calpain inhibitors such as calpeptin. Consistent with a previous study (Boehmerle et al., 2007), we determined that calpain activity increased in a dose-dependent manner in paclitaxel-treated cells (Figure S8D). Second, we observed that treatment with the calpain inhibitor calpeptin impaired paclitaxel treatment-induced MYC loss (Figure S8E) and apoptosis (Figure S8F). Further, the compensatory pERK upregulation seen with paclitaxel treatment was not observed in the calpain inhibitor-treated samples. Ectopic Mut 5 expression impaired siTUBB3-induced MYC loss (Figure S8G), growth suppression (Figure S8H), and paclitaxel-mediated apoptosis (Figures S8I and S8J). Finally, consistent with previous observations (Conacci-Sorrell et al., 2010), confluency stimulated formation of the 33-kDa fragment with WT-MYC-expressing cells, but not Mut-5-MYC-expressing cells (Figure S8K). Taken together, these observations support a mechanism where β-tubulin-inhibition-mediated MYC degradation and apoptosis involve induction of a calpain-mediated MYC degradation mechanism.

We further determined that concurrent treatment with two distinct ERK inhibitors (SCH772984 and ulixertinib) and either baccatin III or paclitaxel caused synergistic loss of MYC and increased apoptosis (Figures 4F–4H, S9A, S9B, and S5E). In summary, these data support a model where β-tubulin inhibition causes calpain-mediated loss of MYC but also induces a DUSP4/6-mediated compensatory ERK activation that drives increased *MYC* transcription, and concurrent ERK inhibition then facilitates synergistic apoptosis.

KX2-391 phenocopies concurrent SRC and β-tubulin inhibition and potently suppresses MYC expression

Because we determined that inhibition of SRC or β-tubulin function enhanced ERK inhibitor activity, we next addressed whether combined inhibition of both would further enhance ERKi efficacy. We evaluated the consequences of concurrent treatment with SRCi and paclitaxel at sublethal concentrations (~GI_{35}). Treatment with the SRCi + paclitaxel combination caused drastic changes in cell morphology that were not observed with treatment with either inhibitor alone, with cells exhibiting a rounded, highly refractile appearance (Figure 5A). Additionally, consistent with our findings that each inhibitor alone caused loss of MYC through distinct mechanisms, the combination treatments potentiated MYC loss (Figure 5B) and caused synergistic apoptosis (Figure 5C). As a complementary approach, we utilized KX2-391 (tirbanibulin), a clinical candidate non-ATP-competitive dual SRC-selective and β-tubulin inhibitor (Niu et al., 2019; Smolinski et al., 2018). We determined if KX2-391 treatment phenocopied concurrent SRCi and paclitaxel treatment of *KRAS* mutant PDAC cells. Like SRCi (Figure 3A), KX2-391 caused a dose-dependent reduction in pp130Cas that correlated directly with a reduction in MYC protein (Figure 5D). However, compared with the SRCi saracatinib, KX2-391 was >10-fold more potent.

Similarly, as we observed with β-tubulin inhibitors (Figures 4B, 4C, and S7I), KX2-391 increased both pHistone H3 (Figure 5D) and G2/M cell-cycle arrest (Figure S9C). Additionally, as with β-tubulin inhibitors (Figures 4B, 4C, and S7I), KX2-391 caused a paradoxical increase in pERK that was associated with loss of DUSP4/6 and decreased levels of MYC protein (Figure 5D). Furthermore, KX2-391 treatment exhibited greater potency in causing loss of MYC protein (Figure 5E) compared with SRCi or β-tubulin inhibitor treatment alone. We conclude that KX2-391 treatment phenocopies the combined signaling and cellular consequences seen with SRCi and paclitaxel treatment and that its two distinct low-potency inhibitory activities against SRC and β-tubulin combine to form the mechanistic basis underlying its ability to drive loss of MYC.

The taxanes baccatin III and paclitaxel enhance microtubule assembly, whereas KX2-391, like vinblastine, inhibits microtubule assembly (Antonarakis et al., 2013; Smolinski et al., 2018). In agreement, we found that KX2-391 reduced microtubule organization (Figure S9D). Similar to baccatin III and paclitaxel (Figure 4E), KX2-391 substantially reduced MYC protein half-life (Figure 5F). We found that MG132 prevented MYC loss induced by paclitaxel alone but only partially rescued the loss of MYC induced by concurrent SRCi and paclitaxel treatment or single-agent KX2-391 (Figure 5G). KX2-391 also caused a limited reduction in *MYC* transcription (Figure S9E). Thus, KX2-391 alone phenocopies concurrent SRCi and paclitaxel treatment and causes loss of MYC through both transcriptional and post-translational mechanisms.

To further evaluate a mechanism for the loss of MYC induced by KX2-391, we performed a time course of KX2-391 treatment. Unlike what we found with ERK inhibition (Figure S3D), we observed that KX2-391 caused an increase in $pMYC^{S62}$ and a decrease in $pMYC^{T58}$ phosphorylation (Figure 5H). However, paradoxically, instead of promoting MYC stability, these phosphorylation changes were instead associated with a reduction in total

MYC protein. These data suggest that KX2-391, like the β-tubulin inhibitors, induced MYC loss through a mechanism distinct from that regulated by FBXW7.

Because KX2-391 exhibits both SRC and β-tubulin-inhibitory activities, it possesses two distinct mechanisms by which it can drive loss of MYC. However, offsetting these mechanisms, β-tubulin-inhibitor-induced compensatory ERK activation prevents FBXW7-dependent MYC degradation and stimulates *MYC* gene transcription. Consistent with a dual mechanism driving MYC loss, we observed biphasic regulation of MYC, such that its abundance was substantially decreased after 4 h of treatment, partially rebounded by 8 h, and was then lost again at 16 and 24 h (Figure 5H). SRCi caused loss of MYC within 1 h (Figure S9F) through suppression of *MYC* transcription (Figure 3C), whereas β-tubulin inhibition caused MYC loss in a more delayed fashion, occurring by 24 h (Figure S9G). We therefore speculate that the initial KX2-391-mediated loss of MYC is likely due to its SRC inhibitory activity. The rebound at 8 h is likely driven by compensatory ERK activation and MYC phosphorylation, which prevents MYC degradation. The subsequent loss of MYC is then likely mediated by β-tubulin inhibition.

KX2-391 synergizes with ERKi to drive robust apoptosis in PDAC and a subset of other cancer types

Despite the potent ability of KX2-391 to drive loss of MYC, its induction of ERK activation through its tubulin-inhibitory function can act as a compensatory resistance mechanism and promote restoration of MYC. Therefore, we evaluated whether concurrent treatment with ERKi could block KX2-391-induced ERK activation and potentiate loss of MYC. KX2-391 alone caused a dose-dependent compensatory increase in pERK activity, as measured by phosphorylation at MYC residue S62 (Figure 6A). This compensatory MYC phosphorylation impaired apoptosis in KX2-391-treated cells (Figure 6B, white bars). Blocking compensatory pERK signaling was associated with a decrease in pMYC^{S62} and a stronger reduction in MYC protein levels (Figure 6A), which resulted in significantly increased apoptosis over single-agent KX2-391 treatment (Figure 6B). A range of KX2-391 and ERKi combinations potently caused both MYC loss and significant, synergistic apoptosis (Figures 6C and 6D). Consistent with both mechanisms of KX2-391, we observed that similar levels of increased apoptosis could be induced by the triple combination of SRCi + paclitaxel + ERKi or the dual combination of KX2-391 + ERKi (Figure 6E). Comparatively, we observed significantly less apoptosis by the dual combination of SRCi + ERKi or the dual combination of paclitaxel + ERKi. The KX2-391 + ERKi combination caused synergistic apoptosis in a panel of *KRAS* mutant PDAC cell lines (Figure 6F) but variable activities when evaluated in breast, head and neck, and lung carcinoma cell lines (Figures S9H–S9J), consistent with the strong *BCAR1* dependency seen in *KRAS* mutant PDAC.

KX2-391 synergizes with ERKi in human PDAC organoids and a syngeneic, orthotopic mouse model of pancreatic cancer

We next evaluated the KX2-391 + ERKi combination in patient-derived *KRAS* mutant PDAC organoids (Tiriac et al., 2018). We performed a matrix dose-response proliferation assay in four patient-derived organoid cultures, and consistent with our observations in

adherent cultures, KX2-391 + ERKi combinations led to synergistic growth suppression by shifting the GI$_{50}$ >2-fold in three out of four organoid lines (Figures 7A and 7B; Table S4).

Next, we transitioned our studies to an *in vivo* setting using a syngeneic, orthotopic mouse model of *Kras*-driven PDAC (Collisson et al., 2012). Tumor-bearing mice were treated for 14 days with vehicle, ERKi (35 mg/kg), KX2-391 (15 mg/kg), or the combination. We note that there may be toxicities observable only in longer-term studies not feasible in this aggressive model, potentially limiting clinical relevance. In particular, targeting the ERK MAPK pathway with MEK inhibitors leads to an increased risk of cardiomyopathy (Flaherty et al., 2012; Kim et al., 2013). However, we found no difference in heart mass in any of the study arms, and the treatment was generally well tolerated, with no significant weight loss (Figures 7C and S10A). Both *in vivo* and *ex vivo* bioluminescence imaging revealed that the combination of KX2-391 and ERKi significantly inhibited pancreatic cancer growth (Figures 7D, 7E, and S10B). Additionally, the size and mass of resected tumors from the single-agent groups were decreased, and the resected tumors from the combination-treated mice were significantly smaller than either single-agent group (Figures 7F and 7G). As we observed using traditional 2D and organoid assays, the combination of KX2-391 and ERKi also induced synergistic growth inhibition in these tumor-bearing mice. Consistent with our *in vitro* observations, KX2-391 alone caused an increase in pHistone and an increase in pERK that was suppressed by concurrent ERK inhibition *in vivo* (Figure S10C). Additionally, while each single-agent treatment reduced MYC, the combination most effectively decreased MYC protein. Thus, we conclude that the observed inhibition of tumor growth was based on the proposed mechanism.

DISCUSSION

Our previous work determined that ERK-independent regulation of MYC is one mechanism of resistance to ERKi (Hayes et al., 2016; Vaseva et al., 2018). In the current study, we identified two such mechanisms. We determined that p130Cas regulates MYC transcriptionally through a SRC-p130Cas-DOCK1-RAC1-β-catenin pathway. We further determined β-tubulin regulates MYC post-translationally through calpain-dependent degradation, and this mechanism is independent of MYC^{S62}. Despite the disparate roles of p130Cas and βIII-tubulin, their mechanisms of supporting PDAC growth converged on regulating MYC, highlighting the critical role of MYC in supporting the KRAS-dependent growth of pancreatic cancer. Exploiting these roles, we established a "triple"-combination therapeutic strategy that concurrently disrupts ERK and p130Cas signaling and microtubule function to potently suppress the tumorigenic growth of PDAC.

In agreement with previous studies, we observed that treatment with microtubule inhibitors caused an increase in phosphorylated and activated ERK. Treatment-induced ERK activation is speculated to drive resistance to microtubule inhibitors. However, there is limited understanding of how microtubule inhibition causes ERK activation. While previous studies suggested ERK activation is mediated through upstream activation of MEK (MacKeigan et al., 2000), our studies here support a mechanism involving loss of the DUSP4/6 protein phosphatases that dephosphorylate and inactivate ERK.

KX2-391 was developed originally as a peptidomimetic-based SRC kinase non-ATP-competitive inhibitor that binds selectively to the SRC peptide substrate domain (Smolinski et al., 2018). Whereas the currently approved ATP-competitive SRC inhibitor dasatinib has activities against at least 68 other protein kinases (Hantschel et al., 2008), KX2-391 is both a more potent and more selective SRC inhibitor. Because KX2-391 is a non-ATP-competitive inhibitor that interferes with the ability of SRC to interact with protein-binding partners (Smolinski et al., 2018), this mode of action helps to mitigate the off-target activities that limit all ATP-competitive protein kinase inhibitors. In agreement with the literature (Liu et al., 2013), we found that KX2-391 is ~30 times more potent than another clinical ATP-competitive SRC inhibitor, saracatinib. Subsequent studies determined a second mode of action for KX2-391, which was disruption of α/β-tubulin heterodimer formation via direct binding to tubulins at a site distinct from conventional microtubule inhibitors (Smolinski et al., 2018; Tu et al., 2012). Therefore, a compound such as KX2-391 provides a unique opportunity to develop a triple combination that utilizes only two pharmacological inhibitors. KX2-391 blocks SRC and microtubule function by mechanisms distinct from the ATP-competitive SRC family inhibitor saracatinib or the microtubule inhibitor paclitaxel. Despite these distinct mechanisms, we found that the two-drug combination of KX2-391 and ERKi largely phenocopied the three-drug combination of saracatinib, paclitaxel, and ERKi in blocking PDAC growth through a MYC-dependent mechanism. Clinical evaluations of KX2-391 have not focused on *KRAS* mutant cancers (Antonarakis et al., 2013; Naing et al., 2013). However, in a phase 1 trial for advanced solid tumors, six patients with PDAC were treated with KX2-391 as monotherapy, and one patient experienced an astounding drop in CA 19–9 levels from 38,838 U/mL to 267 U/mL (Naing et al., 2013).

The interdependency of KRAS and MYC in driving cancer growth is well established (Dang, 2012). Using unbiased genetic screens, we identified functionally divergent vulnerabilities that modulate either KRAS or ERK dependency and converged on the regulation of MYC expression, providing further support that MYC is a key vulnerability of KRAS. Despite the currently undruggable nature of MYC (Dang et al., 2017), our studies suggest that pharmacologic inhibitors of proteins that support MYC expression can be an effective therapeutic strategy to target KRAS-dependent PDAC.

STAR★METHODS

KEY RESOURCES TABLE

REAGENT or RESOURCE	SOURCE	IDENTIFIER
Antibodies		
Rabbit monoclonal anti-p130Cas	Cell Signaling Technology	Cat # 13383
		RRID: AB_2798198
Rabbit polyclonal anti-phospho-p44/42 MAPK (pERK1/2) (Thr202/Tyr204)	Cell Signaling Technology	Cat # 4370
		RRID: AB_2315112
Rabbit polyclonal anti-p44/42 MAPK (ERK1/2)	Cell Signaling Technology	Cat # 9102
		RRID: AB_330744

REAGENT or RESOURCE	SOURCE	IDENTIFIER
Rabbit monoclonal anti-c-MYC (D84C12) XP	Cell Signaling Technology	Cat # 5605
		RRID: AB_1903938
Mouse monoclonal anti-vinculin	Sigma-Aldrich	Cat # V9131
		RRID: AB_477629
Mouse monoclonal anti-KRAS	Sigma-Aldrich	Cat # WH0003845M1
		RRID: AB_1842235
Rabbit monoclonal anti-HA-Tag	Cell Signaling Technology	Cat # 3724
		RRID: AB_1549585
Rabbit polyclonal anti-phospho-RB (Ser780)	Cell Signaling Technology	Cat # 9307
		RRID: AB_330015
Mouse monoclonal anti-phospho-p130Cas (Tyr249)	BD Biosciences	Cat # 558401
		RRID: AB_647286
Rabbit monoclonal anti-p27 Kip1	Cell Signaling Technology	Cat # 3688
		RRID: AB_2077836
Mouse polyclonal anti-PARP	Cell Signaling Technology	Cat # 9542
		RRID: AB_2160739
Mouse monoclonal anti-β-tubulin	Sigma-Aldrich	Cat # T4026
		RRID: AB_477577
Mouse monoclonal anti-β-actin	Sigma-Aldrich	Cat # A5441
		RRID: AB_476744
Rabbit monoclonal anti-phospho-MYC Ser62	Abcam	Cat # 185656
Rabbit monoclonal anti-phospho-RSK1 p90 (Thr359/Ser363)	Cell Signaling Technology	Cat # 9344
		RRID: AB_331650
Rabbit monoclonal anti-RSK1/RSK2/RSK3	Cell Signaling Technology	Cat # 9355
		RRID: AB_659900
Rabbit monoclonal anti-phospho-MEK1/2 (Ser217/221)	Cell Signaling Technology	Cat # 9154
		RRID: AB_2138017
Mouse monoclonal anti-MEK1/2	Cell Signaling Technology	Cat # 4694
		RRID: AB_10695868
Rabbit monoclonal anti-DUSP4	Cell Signaling Technology	Cat # 5149
		RRID: AB_2750867
Rabbit polyclonal anti-DUSP6	Cell Signaling Technology	Cat # 39441
		RRID: AB_2799156
Rabbit monoclonal anti-DOCK180	Cell Signaling Technology	Cat # 4846
		RRID: AB_659284
Rabbit polyclonal anti-ZNF384	Thermo Fisher Scientific	Cat # PA5-52044
		RRID: AB_2650099
Rabbit polyclonal anti-PI3-kinase p110α	Cell Signaling Technology	Cat # 4255
		RRID: AB_659888
Rabbit polyclonal anti-BCAR3	Cell Signaling Technology	Cat # 24032
		RRID: AB_2798871

REAGENT or RESOURCE	SOURCE	IDENTIFIER
Mouse monoclonal anti-RAC1	BD Biosciences	Cat # 610650
		RRID: AB_397977
Rabbit monoclonal anti-non-phospho (active) β-catenin (Ser45)	Cell Signaling Technology	Cat # 19807
		RRID: AB_2650576
Rabbit monoclonal anti-β-catenin	Cell Signaling Technology	Cat # 8480
		RRID: AB_11127855
Rabbit monoclonal anti-βIII-tubulin	Abcam	Cat # ab52623
		RRID: AB_869991
Mouse monoclonal anti-GAPDH	Thermo Fisher Scientific	Cat # MA1-22670
		RRID: AB_559302
Rabbit monoclonal anti-phospho-Histone H3 (Ser10)	Cell Signaling Technology	Cat # 53348
		RRID: AB_2799431
Rabbit polyclonal anti-phospho-c-MYC (Thr 58)	Abcam	Cat # ab28842
		RRID: AB_731667
Mouse monoclonal anti-α-tubulin	Sigma-Aldrich	Cat # T6199
		RRID: AB_477583
Goat anti-rabbit IgG, HRP-linked	Cell Signaling Technology	Cat # 7074
		RRID: AB_2099233
Horse anti-mouse IgG, HRP-linked	Cell Signaling Technology	Cat # 7076
		RRID: AB_330924
Goat anti-Mouse IgG Alexa Fluor 488	Thermo Fisher Scientific	Cat # A-32723
		RRID: AB-2633275
Bacterial and virus strains		
DH5α	Thermo Fisher Scientific	Cat# 18258012
Chemicals, peptides, and recombinant proteins		
Human Druggable Genome siRNA Library v3	QIAGEN	N/A
SCH772984 (ERK1/2 inhibitor)	Provided by Merck	N/A
Saracatinib (SRC inhibitor)	Selleckchem	Cat # S1006
Cycloheximide (translation inhibitor)	Sigma-Aldrich	Cat # C4859
Baccatin III (antimitotic)	Sigma-Aldrich	Cat # B8154
Paclitaxel (antimitotic)	Selleckchem	Cat # S1150
Vinblastine (tubulin inhibitor)	Selleckchem	Cat # S4505
KX2-391 (SRC/tubulin inhibitor)	Selleckchem	Cat # S2700
MG132 (proteasome inhibitor)	Sigma-Aldrich	Cat # M7449
DAPI	Thermo Fisher Scientific	Cat # D3571
RNase A	Thermo Fisher Scientific	Cat # EN0531
Propidium iodide	Thermo Fisher Scientific	Cat # P3566
2-hydroxypropyl-β-cyclodextrin	Sigma-Aldrich	Cat # H107
Matrigel Growth Factor Reduced Basement Membrane Extract, Phenol Red-free, LDEV-free	Corning	Cat # 356231

REAGENT or RESOURCE	SOURCE	IDENTIFIER
Matrigel Basement Membrane Matrix, Phenol Red-free, LDEV free	Corning	Cat # 356237
XeonLight D-Luciferin -K+	Perkin Elmer	Cat # 122799
Critical commercial assays		
TACS Annexin V-FITC *in situ* apoptosis detection kit	Trevigen, Inc.	Cat # 4830
CellTiter-Glo Luminescent Cell Viability Assay	Promega	Cat # G7570
CellTiter-Glo 3D Cell Viability Assay	Promega	Cat # G9683
Calpain Activity Fluorometric Assay Kit	BioVision, Inc.	Cat # K240
Deposited data		
siRNA druggable genome ERKi sensitivity screen	This study	Table S1
KRAS dependency analysis of CRISPR-Cas9 screening data	Tsherniak et al., 2017	Release code 20Q1
Multiplexed kinase inhibitor beads and mass spectrometry with siBCAR1 treatment	This study	Table S2 Figure S2B
Experimental models: cell lines		
Human: Pa01C (pancreatic ductal adenocarcinoma)	Jones et al., 2008	N/A
Human: Pa02C (pancreatic ductal adenocarcinoma)	Jones et al., 2008	N/A
Human: Pa03C (pancreatic ductal adenocarcinoma)	Jones et al., 2008	N/A
Human: Pa04C (pancreatic ductal adenocarcinoma)	Jones et al., 2008	N/A
Human: Pa14C (pancreatic ductal adenocarcinoma)	Jones et al., 2008	N/A
Human: Pa16C (pancreatic ductal adenocarcinoma)	Jones et al., 2008	N/A
Human: AsPC-1 (pancreatic ductal adenocarcinoma)	ATCC	Cat # CRL-1682
		RRID: CVCL_0152
Human: SW 1990 (pancreatic ductal adenocarcinoma)	ATCC	Cat # CRL-2172
		RRID: CVCL_1723
Human: HPAC (pancreatic ductal adenocarcinoma)	ATCC	Cat # CRL-2119
		RRID: CVCL_3517
Human: MIA PaCa-2 (pancreatic ductal adenocarcinoma)	ATCC	Cat # CRL-1420
		RRID: CVCL_0428
Human: PANC-1 (pancreatic ductal adenocarcinoma)	ATCC	Cat # CRL-1469
		RRID: CVCL_0480
Human: HPNE-DT (pancreatic epithelium)	Campbell et al., 2007	N/A
Human: HPNE RAS (transformed pancreatic epithelium)	Campbell et al., 2007	N/A
Human: MDA-MB-231 (breast adenocarcinoma)	ATCC	Cat # HTB-26
		RRID: CVCL_0062
Human: BT-549 (breast ductal carcinoma)	ATCC	Cat # HTB-122
		RRID: CVCL_1092
Human: HCC70 (breast ductal carcinoma)	ATCC	Cat # CRL-2315
		RRID: CVCL_1270
Human: UM-SCC-4 (tongue squamous cell carcinoma)	Brenner et al., 2010	RRID: CVCL_7751

REAGENT or RESOURCE	SOURCE	IDENTIFIER
Human: UM-SCC-11A (laryngeal squamous cell carcinoma)	Brenner et al., 2010	RRID: CVCL_7715
Human: KYSE30 (esophageal squamous cell carcinoma)	ATCC	Cat # HTL97022
		RRID: CVCL_1351
Human: H2228 (non-small cell lung adenocarcinoma)	ATCC	Cat # CRL-5935
		RRID: CVCL_1543
Human: H358 (non-small cell lung adenocarcinoma)	ATCC	Cat # CRL-5807
		RRID: CVCL_1559
Human: H23 (non-small cell lung adenocarcinoma)	ATCC	Cat # CRL-5800
		RRID: CVCL_1547
Human: HEK293T (embryonic kidney, expressing SV40 T antigen)	ATCC	Cat # CRL-3216
		RRID: CVCL_0063
Mouse: p53 2.1.1$^{syn\_Luc}$ (KP) (pancreatic ductal adenocarcinoma)	Collisson et al., 2012	N/A
Mouse: INK4.1$^{syn\_Luc}$ (KI) (pancreatic ductal adenocarcinoma)	Collisson et al., 2012	N/A
Experimental models: organisms/strains		
Human: hM1A PDAC organoid	Boj et al., 2015	N/A
Human: hT2 PDAC organoid	Boj et al., 2015	N/A
Human: hT105 PDAC organoid	Tiriac et al., 2018	N/A
Human: hT106 PDAC organoid	Tiriac et al., 2018	N/A
Mouse: FVB/n strain	The Jackson Laboratory	Cat # 001800
p53 2.1.1$^{syn\_Luc}$ Kras^{G12D}/p53$^{-/-}$ orthotopic, syngeneic mouse model (FVB/n strain)	Collisson et al., 2012	N/A
Oligonucleotides		
See Table S5		N/A
Recombinant DNA		
Empty Vector	Martz et al., 2014	N/A
MYC WT	This study	N/A
MYC T58A	This study	N/A
MYC S62A	This study	N/A
MYC Mutant 1 (S71A, S81A, S159A)	This study	N/A
MYC Mutant 2 (T58A, S62A, S71A, S81A)	This study	N/A
MYC Mutant 3 (Δ1-149)	This study	N/A
MYC Mutant 4 (T343A, S344A, S347A, S348A)	This study	N/A
MYC Mutant 5 (S151A, S159A, S161A)	This study	N/A
MYC Mutant 6 (S303A, T304A, S314A, S315A)	This study	N/A
MYC Mutant 7 (S279A, S281A, S283A, S293A)	This study	N/A
MYC Mutant 8 (S277A, S279A, S281A, S283A, S288A, S293A, S303A, T304A, S314A, T315A)	This study	N/A
MYC Mutant 9 (K298R, K317R, K323R, K326R, K340R)	This study	N/A

REAGENT or RESOURCE	SOURCE	IDENTIFIER
MYC Mutant 10 (K51R, K52R, K126R, K143R, K148R, K157R)	This study	N/A
β-catenin 4A (S33A, S37A, T41A, S45A)	Martz et al., 2014	N/A
pBV-Luc wt MBS1-4	Hermeking et al., 2000	Addgene Cat # 16564
Software and algorithms		
ImageLab version 2.2.4.0	Bio-Rad	https://www.bio-rad.com/en-us/product/image-lab-software?ID=KRE6P5E8Z
MATLAB	The Mathworks, Inc.	https://www.mathworks.com
ZEN (blue software) version 2.3	Zeiss	https://www.zeiss.com/microscopy/us/products/microscope-software/zen.html
GraphPad Prism version 6.0	GraphPad	https://www.graphpad.com/scientific-software/prism/
Ingenuity Pathway Analysis version 01.12	QIAGEN	https://digitalinsights.qiagen.com/products-overview/discovery-insights-portfolio/content-exploration-and-databases/qiagen-ipa/.
FCS Express version 7.0	De Novo Software	https://denovosoftware.com/
Cytobank version 7.3.0	Kotecha et al., 2010	https://www.cytobank.org/
FACSDiva v8.0.1	BD Biosciences	https://www.bdbiosciences.com/en-us
Python version 3.7.4	Python Software Foundation	https://www.python.org/
ImageJ version 2.0.0-rc-69/1.52n	Schneider et al., 2012	https://imagej.nih.gov/ij/
DEMETER	Tsherniak et al., 2017	https://depmap.org/portal
STRING	Szklarczyk et al., 2015	https://string-db.org
R (version 3.5.1)	R Core Team, 2013	https://www.R-project.org/
KRAS dependency volcano plots	This study	https://github.com/kkapner/watersetalmyc
Other		
MYC QPCR primer	Thermo Fisher Scientific	HS00153408_m1
β-actin QPCR primer	Thermo Fisher Scientific	4310881E-1711049

RESOURCE AVAILABILITY

Lead contact—Further information and requests for resources and reagents should be directed to and will be fulfilled by the lead contact, Channing J. Der (cjder@med.unc.edu).

Materials availability—This study did not generate new unique reagents.

Data and code availability—This study did not generate any unique codes.

EXPERIMENTAL MODEL AND SUBJECT DETAILS

Cell culture—The patient-derived xenograft human pancreatic cancer cell lines Pa01C, Pa02C, Pa03C, Pa04C, Pa14C and Pa16C were gifted by Dr. Anirban Maitra (MD Anderson Cancer Center). p53 2.1.1$^{syn\_Luc}$ (KP) and INK4.1$^{syn\_Luc}$ (KI) mouse pancreatic cancer cell lines were gifted by Dr. Eric Collisson (University of California – San Francisco). Conventional human pancreatic cancer cell lines (AsPC-1, SW 1990, HPAC, MIA PaCa-2, PANC-1), breast cancer cell lines (MDA-MB-231, BT-549, HCC70), head and neck cancer cell line (KYSE30), and lung cancer cell lines (H2228, H358, H23) were obtained from American Type Culture Collection (ATCC). Head and neck cancer cell lines (UM-SCC-4, UM-SCC11a) were acquired from the University of Michigan, Ann Arbor, through a Material Transfer Agreement. All cell lines were cultured at 37°C and 5% CO_2 in a humidity-controlled incubator and maintained in Dulbecco's Modified Eagle medium (DMEM), or Roswell Park Memorial Institute medium (RPMI) supplemented with 10% fetal bovine serum (FBS). Cell lines were tested negative for mycoplasma and identities were authenticated by Short Tandem Repeat (STR) analysis.

Patient derived PDAC organoids—The human pancreatic cancer organoids were provided by Dr. David Tuveson (Cold Spring Harbor Laboratory). The patient derived PDAC organoids were cultured at 37°C in 5% CO_2. Cells were initially seeded in growth factor reduced Matrigel (Corning) domes and after reseeding were fed with complete human feeding medium: advanced DMEM/F12 (Thermo Fisher Scientific) based WRN conditioned medium (L-WRN (ATCC CRL-3276)), 1x B27 supplement (Thermo Fisher Scientific), 10 mM HEPES (Thermo Fisher Scientific), 0.01 μM GlutaMAX (Thermo Fisher Scientific), 10 mM nicotinamide (Sigma-Aldrich), 1.25 mM N-acetylcysteine (Sigma-Aldrich), 50 ng/mL hEGF (Peprotech), 100 ng/mL hFGF10 (Peprotech), 0.01 μM hGastrin I (TOCRIS), 500 nM A83-01 (TOCRIS), and 10.5 μM Y27632 (Selleckchem) (Boj et al., 2015). Organoids were tested negative for mycoplasma.

Mice—FVB/N female mice (n = 36, 7 weeks old) were purchased from The Jackson Laboratory and cared for according to guidelines set forth by the American Association for Accreditation of Laboratory Animal Care and the U.S. Public Health Service policy on Human Care and Use of Laboratory Animals. All mouse studies were approved and supervised by the Institutional Animal Care and Use Committee of the University of North Carolina at Chapel Hill. Animals were allocated to four equal groups based on a baseline IVIS imaging 7 days after tumor implantation. Each group had similar average IVIS signals prior to the start of treatment.

METHOD DETAILS

siRNA druggable genome ERKi sensitization screen—Four siRNA sequences for each gene from The Human Druggable Genome v3 siRNA Library (QIAGEN) were selected for screening in 90 384-well plates. All assay plates included negative control siRNAs (Non-Silencing, All-Star Non-Silencing, and GFP), and two positive control siRNAs (UBBs1 and All-Star Cell Death Control). The siRNAs were printed individually into solid white 384-well plates (1 μL of 0.667 μM siRNA per well for a total of 9 ng siRNA). Lipofectamine RNAiMax (Thermo Scientific) was diluted in serum-free medium and 20 μL was transferred into each well of the 384-well plate containing siRNAs. After a 30 min incubation at room temperature, 750 Pa16C cells were added in 20 μl into each well. After 24 hr, DMSO or various concentrations of ERKi was added. Cells were then incubated at 37°C for 96 hr. Cell viability was measured using the CellTiter-Glo.

To normalize raw outputs from the plate reader, raw data values for every plate were divided by the median of the same plate's compound free non-transfected wells and scaled to the controls. Effectiveness of siRNA knockdown was assessed by comparing normalized signal in wells transfected with positive-control (All-Star Cell Death Control and UBBs1) and negative-control (GFP) siRNAs in the absence of compound intervention. Transfection efficiency, which was calculated as percent decrease of the median of positive controls compared to the median of the negative controls, was above 99%. The screen met previously established statistical parameters for rigor, with a coefficient of variance of < 10% in the negative controls and a Z-factor above 0.8 (Zhang et al., 1999). Finally, coefficient of variation of the negative controls in the absence of compound treatment was below 10%. Activity of each siRNA was summarized with slope, top, bottom and GI_{50} parameters calculated by fitting normalized data across 8 compound concentrations to a sigmoidal dose-response curve using a custom MATLAB script.

We identified 2,336 siRNAs as toxic with either a GI_{50} below the lowest concentration tested or with normalized signal below 70% of the signal level representing wells where the compound was absent. 473 genes with at least two toxic siRNAs were excluded from further analysis. Redundant siRNA activity (RSA) (König et al., 2007) was applied to integrate the activity of multiple siRNAs targeting each gene. Out of 297 selected genes that had p values < 0.05, we further prioritized 240 genes for a follow up confirmation screen, based on normal or high expression in the screening cell line. All four siRNA sequences for each of the 240 genes were selected to create three custom 384-well assay plates. The preparation of the confirmation screen plates, the addition of transfection reagent, cells, ERKi, and CellTiter-Glo® were all performed in the same manner as described in the primary screen and raw plate reader outputs were normalized as described above. Hits were defined as genes that had at least two siRNAs with above a threefold shift in the GI_{50} in the ERKi dose-response curve compared to controls.

KRAS dependency analysis of CRISPR-Cas9 screening data—To identify KRAS synthetic lethal interactions, we analyzed existing data from the Cancer Dependency Map (version 20Q1; https://www.depmap.org/portal) (Tsherniak et al., 2017). For the comparison of KRAS mutant versus KRAS WT cell lines (Meyers et al., 2017), cell lines were grouped

according to KRAS mutant or wild-type status. We then performed a two-tailed t test for each gene between the KRAS mutant and KRAS WT groups. The mean CERES score (Meyers et al., 2017) for each gene was then found for the KRAS mutant and KRAS WT cell lines respectively. As described previously, the CERES score is necessary to account for gene-independent proliferative defects inherent in Cas9-mediated DNA cleavage (Meyers et al., 2017). For each gene, the difference between the CERES scores between the two groups and the $-\log_{10}$ of the p value from the corresponding two tailed t test were plotted on the x- and y-axes, respectively. The absolute values of the CERES differences below zero are shown.

For the comparison of CRISPR-Cas9 dependencies in the KRAS-dependent pancreatic cell lines versus KRAS-independent non-pancreatic cell lines, we used available RNAi dependency data (Tsherniak et al., 2017) and defined two groups: 1) KRAS dependent pancreatic cell lines (taken as all pancreas lines with an RNAi DEMETER2 score < −0.5 for KRAS) and KRAS independent non-pancreatic cell lines (taken as all non-pancreas lines with an RNAi DEMETER2 score > −0.5 for KRAS). We again performed a two-tailed t test between the groups and plotted the data as a volcano plot. DEMETER2 scores, as described previously (McFarland et al., 2018), allow integrated analysis of multiple genome-scale viability screens across hundreds of cancer cell lines and account for known RNAi off-target seed effects.

For the correlation analysis, all cell lines found in the Cancer Dependency Map dataset (Version 20Q1) were used to calculate the Pearson correlation with *BCAR1* dependency. All Pearson correlations were then z-scored and sorted in descending order. The top 25 correlated genes with *BCAR1* were then used to generate the network diagram using https://string-db.org and Cytoscape (Szklarczyk et al., 2015).

Gene essentiality analyses—To identify genetic dependencies across cancer types, we analyzed existing data from the PICKLES database using the Avana 2018Q4 dataset (Meyers et al., 2017; Lenoir et al., 2018). PICKLES "essentiality scores" are generated using BAGEL (Hart and Moffat, 2016) to produce Bayes factors (BF) from log-fold fold change data obtained through the Cancer Dependency Map. Cell lines were then stratified by cancer type and KRAS mutational status. The threshold for essentiality was set at BF = 5 in accordance with PICKLES guidelines.

shRNA lentiviral infections and siRNA transfections—All shRNAs were provided in glycerol stock form by the UNC School of Medicine Lenti-shRNA Core Facility. After purifying the shRNA-containing plasmid DNAs, 12 μg were mixed with psPAX2 (9 μg) and pMD2.G (3 μg) and subsequently diluted in 1 mL of Opti-MEM medium. FuGENE HD (62 μl) was added into the diluted plasmid mixture and incubated for 8–10 min at room temperature before the transfection mixture was added to 5×10^6 HEK293T cells that were seeded the prior day in a T75 flask. Transfection medium was replaced with DMEM + 10% FBS the next day and incubated an additional 48 hr. Virus particles were filtered in a 0.45 μm filter, collected, and frozen at −80°C. Cells (8×10^5) plated in a T25 flask were infected by combining 0.5 mL of virus with 8 μg/ml polybrene in 3 mL of medium. The medium was replaced with DMEM + 10% FBS the next day. Puromycin antibiotic selection was started

after an additional 24 hr. After 72 to 120 hr of antibiotic selection, cells were collected for immunoblotting, proliferation, clonogenic, cell cycle, or apoptosis assays.

siRNAs were purchased from Dharmacon. Before siRNA transfection, 2×10^5 cells were seeded into one well of a 6-well plate. The next day, culture medium was replaced. To suppress *BCAR1*, 25 pmol of siRNA were added to 200 μl of Opti-MEM medium followed by 2.5 μl of RNAiMax. To suppress *TUBB3*, 30 pmol of siRNA were added to 200 μl of Opti-MEM medium followed by 9 μl of RNAiMax. The mixtures were incubated for 8–10 min before being added dropwise to cells. The next day, cells were collected for immunoblotting, proliferation, clonogenic, or apoptosis assays.

Immunoblotting—Cells were washed twice with ice-cold PBS, lysed with ice-cold 1% Triton X-100 buffer (20 mM Tris-HCl, 150 mM NaCl, 1 mM EDTA) supplemented with protease (Roche) and phosphatase (Sigma-Aldrich) inhibitors, and incubated 10 min on ice before scraping the lysates into pre-chilled tubes. For cycloheximide chase and MG132, for half-life and proteasomal degradation experiments, respectively, 2×10^5 cells were seeded into 6-well plates. After 20 hr of 10 μg/ml cycloheximide or 5 μM MG132 treatment, inhibitors were added for the indicated times before lysing cells and performing immunoblots. Cell lysates were centrifuged at 18,213 x g for 15 min at 4°C, and the supernatant was collected for determining protein concentration by bicinchoninic (BCA) assay (Pierce) using BSA as a standard. Equal protein concentrations were loaded onto each gel (15 μg). Standard immunoblotting procedures were followed. Nitrocellulose membranes were activated with methanol and membranes were blocked in 3% milk diluted in TBST (TBS with 0.05% Tween 20) for 1 hr. Wet transfers were performed at 100V for 75 min at room temperature. Protein levels were quantified by densitometric intensity. All quantification was performed with ImageJ.

RAC1-GTP pulldown—RAC1-GTP pulldowns were performed using the GST-PAK protein binding domain attached to Sepharose beads (Cytoskeleton) essentially as described by the manufacturer's recommended protocol. Each pulldown was performed with 150 μg of cell lysate combined with 15 μg of Sepharose beads and rotated for 1 h at 4°C. After washing, the samples were suspended in loading dye and analyzed by SDS-PAGE and immunoblot.

RT-qPCR—Cells were grown in 6-well plates, treated with drug as indicated, and harvested. RNA was extracted using the RNeasy Isolation Kit (QIAGEN) and converted to cDNA using the High-Capacity cDNA Reverse Transcription Kit (Applied Biosystems). RT-PCR was performed using the TaqMan system (Applied Biosystems) in a 384-well format. FAM-labeled target primer and endogenous control (VIC-B-Actin) were mixed with master mix and template, and after 40 cycles were analyzed on an Applied Biosystems QuantStudio 6.

Proliferation assays—For siRNA transfections, cells (3×10^3) were seeded in 96-well plates and incubated for 72–120 hr. If necessary, the day after seeding, small molecule inhibitors were added alone or in combination, as indicated. Proliferation was measured by

incubating each well with 500 nM calcein-AM and incubating for 30 min before reading in a SpectraMax i3x multimode plate reader.

Clonogenic assays—PDAC cells were seeded at single-cell density (5×10^3 to 1.5×10^4 cells per well, according to the cell line) in 6-well plates. After 10–14 days, colonies were fixed with 4% paraformaldehyde and stained with 0.1% crystal violet. For siRNA experiments, cells were seeded into 6-well plates 24 hr after the transfection.

Organoid proliferation assays—PDAC organoids were dissociated and 3×10^3 cells were seeded in 150 µl of 10% growth factor reduced Matrigel (Corning) and 90% human organoid feeding media + 10.5 µM Y27632 (Selleckchem) into 96-well clear flat bottom plates (Corning) coated with poly(2-hydroxyethyl methacrylate) (Sigma-Aldrich). On the second day after seeding, organoids were drugged with ERKi (SCH772984, 0.025 to 2.5 µM) and/or KX2-391 (15.75 to 62.5 nM) using a Tecan D300e digital dispenser. Seven days after drugging, organoids were imaged with a Molecular Devices SpectraMax i3x MiniMax 300 imaging cytometer. After image acquisition, organoid viability was assessed with the CellTiter-Glo® 3D Cell Viability Assay (Promega) on a SpectraMax i3x plate reader, according to the manufacturer's protocol.

Flow cytometry—For apoptosis assays, the TACS Annexin V-FITC Apoptosis Detection Kit (Trevigen, Inc.) was used to measure apoptosis according to the manufacturer's instructions. Detached cells in the spent culture medium and the trypsinized cells were collected, mixed, and centrifuged at $300g$ for 5 min at room temperature. The cells were washed with PBS and centrifuged at $300g$ for 5 min before incubating the cell pellet in Annexin V Incubation Reagent (1% Annexin V-FITC, 1x propidium iodide solution, in 1x calcium-containing binding buffer) in the dark for 15 min at room temperature. Cell mixture was diluted 1:5 in 1x binding buffer. For cell cycle analysis, cells were trypsinized and centrifuged at $300g$ for 5 min before washing once in PBS. Cells were pelleted and resuspended in PBS before adding 9 volumes of 70% ethanol drop-wise to each tube with gentle agitation. Cells were fixed overnight at 4°C. The next day, cells were pelleted, washed once in PBS, resuspended in 40 µg/ml propidium iodide (PI), 100 µg/ml RNase A in PBS, and incubated at 37°C for 3 hr. A BD LSRFortessa flow cytometer was used for analysis. FACSDiva v8.0.1 was used to collect and export 3×10^4 cells. Apoptosis assays were analyzed with Cytobank. A FSC-A versus SSC-A dot plot was used to exclude debris and generate a "cells" gate. "Cells" were plotted in a FITC-A (x) versus PI-A (y) dot plot and apoptotic cells (FITC+) were analyzed. Cell cycle analyses were performed with FCS Express. After establishing a "cells" gate, a "singlets" gate was determined using a FSC-A (x) versus FSC-H (y) dot plot. Singlets were then analyzed in a histogram for PI-A content before employing the Multicycle algorithm to analyze cell cycle.

MYC reporter activity assay—To monitor *MYC* transcriptional activity, 5×10^3 cells were seeded in white, clear-bottomed 96-well plates. After 48 hr, the cells were transfected with pBV-Luc wt MBS1-4 MYC-responsive luciferase reporter at a 1:1 ratio of mg DNA:TransIT-2020 transfection reagent (Mirus Bio) per well. Proliferation was measured by incubating each well with 500 nM calcein AM and incubating for 30 min before reading in a

SpectraMax i3x multimode plate reader. Luminescence values were proliferation-normalized and then normalized to the empty vector control.

Calpain activity assay—To measure calpain activity, a Calpain Activity Fluorometric Assay Kit (Biovision, Inc.) was used. Briefly, 2×10^5 Pa16C cells were seeded into 6-well plates and treated with increasing doses of paclitaxel for 48 hr before performing the fluorometric calpain activity assay in accordance with the manufacturer's instructions.

MYC rescue experiments—Virus particles were produced as described above for the pCDH MYC constructs. Pa16C cells (5×10^5) plated in a T25 flask were infected by combining 0.5 mL of virus with 8 μg/ml polybrene in 3 mL of medium. The medium was replaced with DMEM supplemented with 10% FBS the next day. After an additional 24 hr, cells were harvested and seeded into T75 flasks in the presence of 2 μg/ml puromycin. After 72 hr, puromycin concentration was halved (1 μg/ml) and cells were selected for an additional 15 days (due to differential toxicity of the constructs to the infected cells) until they were seeded into assays.

For *BCAR1* and *TUBB3* rescue experiments, 2×10^5 Pa16C cells were seeded into 6-well plates, and the next day transfected with control nonspecific (NS) siRNA, siBCAR1, or siTUBB3. The next day, the growth medium was replaced with fresh grown medium. The following day, cells were harvested, and 2×10^5 cells were seeded into 6-well plates for immunoblot analyses as described above, and 3×10^3 cells were seeded into 96-well plates for 72 hr proliferation assays as described above.

For paclitaxel-mediated MYC rescue experiments, 1.5×10^5 cells for each infected Pa16C cell line were plated into 6-well plates before 2.5 nM paclitaxel addition the next day. Cells were harvested for apoptosis assays 72 hr after paclitaxel treatment and apoptosis assays were performed as described above. For cycloheximide and calpeptin experiments, 2×10^5 cells were plated into 6-well plates and treated as described above.

Activated β-catenin rescue experiments—Virus particles were produced as described above for the pCW317 EV and 4A constructs. Cells (5×10^5) plated in a T25 flask were infected the next day by combining 0.5 mL of EV or 4A virus with 8 μg/ml polybrene in 3 mL of medium. The medium was replaced with DMEM + 10% FBS the next day. After an additional 24 hr, cells were harvested and seeded into T75 flasks in the presence of 2 μg/ml puromycin. After 72 hr, 5×10^5 EV- or 4A-infected cells were seeded into multiple T25 flasks. Cells were infected the next day with shRAC1 or shDOCK1 by combining 0.5 mL of EV or 4A virus with 8 μg/ml polybrene in 3 mL of medium. The medium was replaced with DMEM supplemented with 10% FBS the following day. The following day, cells were harvested, and 2×10^5 cells were seeded into 6-well plates for immunoblot analyses, 3×10^3 cells were seeded into 96-well plates for 72 hr proliferation assays, and 1.5×10^3 cells were seeded into 6-well plates for clonogenic assays, as described above.

Multiplexed inhibitor beads/mass spectrometry (MIB/MS)—Pa16C cells were treated nonspecific siRNA (siNS) or *BCAR1*-targeting siRNAs for 72 hr to monitor the kinome response. The samples were prepared as described previously (Duncan et al., 2012).

Briefly, the cells were lysed on ice with MIB lysis buffer [50 mM HEPES (pH 7.5), 0.5% Triton X-100, 150 mM NaCl, 1 mM EDTA, 1 mM EGTA, 10 mM sodium fluoride, 2.5 mM sodium orthovanadate, 1 protease inhibitor cocktail (Roche), 1% phosphatase inhibitor cocktail 2 (Sigma-Aldrich), and 1% phosphatase inhibitor cocktail 3 (Sigma-Aldrich)]. The cell lysates were sonicated (3×10 s, 50% pulse) and clarified by centrifugation (> 10,000 x g) at 4°C for 10 min. The supernatant was filtered through a 0.2 μm filter. The lysates (~2 mg protein per sample) were brought to 1 M NaCl and flowed over a column containing multiplexed kinase inhibitor beads (MIBs) (Sepharose conjugated to VI-16832, CTx-0294885, PP58, Purvalanol B, UNC8088A, UNC21474). MIBs were washed sequentially with a high salt buffer [50 mM HEPES (pH 7.5), 0.5% Triton X-100, 1 M NaCl, 1 mM EDTA, 1 mM EGTA], a low salt buffer [50 mM HEPES (pH 7.5), 0.5% Triton X-100, 150 mM NaCl, 1 mM EDTA, 1 mM EGTA], and a low salt + 0.1% SDS buffer. The samples were boiled with the elution buffer (100 mM Tris-HCl, 0.5% SDS, and 1% β-mercaptoethanol, pH 6.8) at 100°C for 5 min to elute the bound kinases from MIBs. The eluted kinases were reduced [dithiothreitol], alkylated [iodoacetamide] and then concentrated with Amicon Ultra-4 (10K cutoff) spin columns (Millipore). Kinases were purified by removing the detergent using methanol/chloroform extraction and digested with trypsin (Promega) overnight at 37°C. Hydrated ethyl acetate extraction was used to remove Triton, and PepClean C-18 spin columns (Pierce, Thermo Fisher Scientific) were used to de-salt the digested peptides.

LC/MS/MS—The peptide samples were analyzed by LC/MS/MS using a Waters nanoAcquity coupled to a Thermo Fusion Lumos mass spectrometer. Samples were injected onto a Thermo PepMap C18 trap column, washed, and then loaded onto an Easy Spray PepMap C18 analytical column (75 μM id × 25 cm, 2 μM particle size) (Thermo Scientific). The samples were separated over a 120 min method, where the gradient for separation consisted of 2%–25% mobile phase B at a 300 nl/min flow rate; mobile phase A was 0.1% formic acid in water and mobile phase B consisted of 0.1% formic acid in 100% acetonitrile. MS1 orbitrap scans were collected at a resolution of 120,000 and 1e6 AGC target. The MS2 spectra were acquired either in the orbitrap or the linear ion trap depending on peak charge and intensity using a 3 s TopSpeed CHOPIN method (Davis et al., 2017). Orbitrap MS2 scans were acquired at 7500 resolution, with a 5e4 AGC, and 22ms maximum injection using HCD fragmentation with a normalized energy of 30%. Rapid linear ion trap MS2 scans were acquired using a 4e3 AGC, 250 ms maximum injection time, CID fragmentation set at 30%. Dynamic exclusion was set to 30 s and precursors with unknown charge or a charge state of 1 and ≥ 8 were excluded.

Immunofluorescence—Pa16C cells were plated on glass-bottom 12-well MatTek plates and treated as indicated. The cells were fixed and permeabilized with 100% ice-cold MeOH and incubated on ice for 15 min. Cells were washed three times with PBS before blocking with Odyssey blocking buffer (Li-Cor) for 30 min and incubated overnight with a 1:500 dilution of anti-α-tubulin antibody in blocking buffer. Cells were washed with blocking buffer, incubated for 1 hr in Goat anti-Mouse Alexa Fluor 488, counterstained with DAPI for 10 min and then washed three times with PBS. Cells were imaged on a Zeiss LSM710 confocal microscope with a 40x oil objective. For quantitation, 30–60 cells per condition

were analyzed using the Zeiss Zen Blue software and ImageJ. Z stacks of each field were used to calculate the maximum intensity projection. Tubulin levels were determined based on the corrected total cell fluorescence intensity of the maximum intensity projection for each cell, corrected for cell size and background. The corrected total cell fluorescence was calculated as integrated density of the cell (cell area × mean fluorescence of background readings).

Mouse studies—To evaluate concurrent ERKi and KX2-391 treatment *in vivo*, luciferase-expressing p53 2.1.1$^{syn\_Luc}$ mouse pancreatic tumor-derived cells (*Kras^{G12D}*, *tp53$^{-/-}$*) (Collisson et al., 2012) were kindly provided by Eric Collisson (University of California, San Francisco). Mice were acclimated for one week prior to implantation. After three passages in traditional cell culture, cells were trypsinized, washed, and resuspended in 50% Hanks' balanced salt solution (GIBCO), 50% LDEV-free Matrigel (Corning) at a concentration of 25 cells/μl, and kept on ice. Cells (40 μl, 1×10^3 cells/mouse) were then implanted into the head of the pancreas of 36 adult mice. Ketamine (80 mg/kg), xylazine (8 mg/kg), and acepromazine (1 mg/kg) were used to anesthetize the mice prior to surgery. A tuberculin syringe with a 30-g needle was inserted into an abdominal incision and used for implantation. The incision was closed using surgical staples. After a one-week recovery, initial IVIS imaging with D-luciferin substrate (Perkin Elmer) was performed using an IVIS Lumina optical imaging system. Mice were separated into four equal groups (n = 9 mice per group) based on equal average luciferase signal. The four groups were then treated daily for an additional two weeks with vehicle, 35 mg/kg ERKi IP, 15 mg/kg KX2-391 PO, or the combination. The vehicle group was treated daily with the solvents for ERKi and KX2-391: 20% 2-hydroxypropyl-β-cyclodextrin (Sigma-Aldrich), 100 μl IP; and/or 5% DMSO/95% distilled water, 200 μl PO, respectively. IVIS imaging was performed in the middle and at the end of the study. Mice were sacrificed at the conclusion of the study, the pancreas was removed, and *ex vivo* bioluminescence imaging was performed. Tumors were then excised from the pancreas and weighed.

QUANTIFICATION AND STATISTICAL ANALYSIS

Synergy calculations—A Bliss independence model (Foucquier and Guedj, 2015) was performed for all assays assessing synergy using the formula CI = $(E_A + E_B - E_A E_B)/E_{AB}$ (CI = combination index, E_A = treatment one effect, E_B = treatment two effect, E_{AB} = combination effect).

Statistical analysis—Two-tailed Student's t tests (assuming equal variance) were performed for all assays with statistical data, and data are presented as mean values ± standard deviation unless otherwise noted. Confidence intervals were denoted with one (p value < 0.05), two (p value < 0.01), three (p value < 0.001), or four (p value < 0.0001) asterisks in the appropriate figure panels. Statistical details of particular experiments can be found in the figure legends.

MIB/MS analysis—Raw data files were processed using MaxQuant and searched against the reviewed human database (downloaded Jan 2019, containing 20,414 entries), using Andromeda within MaxQuant. Enzyme specificity was set to trypsin, up to two missed

cleavage sites were allowed, carbamidomethylation of C was set as a fixed modification and oxidation of M and acetyl of N-term were set as variable modifications. A 1% false discovery rate was used to filter all data and match between runs was enabled. A minimum of two peptides was required for label-free quantitation using the label-free quantitation (LFQ) intensities.

Data files were analyzed using R (version 3.5.2). A total of 197 kinases were identified with 183 kinases present in > 50% of samples and containing two or more peptides. Fifty of 191 kinases were missing 1 or more values after this filtering and these values were imputed. A normal distribution was modeled on the non-missing LFQ intensity values of the kinases containing missing intensity values. Imputed values were drawn randomly from this distribution. Following filtering and imputation, LFQ intensity values were log2 transformed and the fold change over the median vehicle value was calculated for each kinase. Significant kinases between siNS, siBCAR1 A, and siBCAR1 D conditions were determined using one-way ANOVA (Benjamini-Hochberg adjusted p value < 0.05). Euclidean distance and average linkage were utilized for unsupervised hierarchical clustering of log2 fold-change values for significant kinases.

Supplementary Material

Refer to Web version on PubMed Central for supplementary material.

ACKNOWLEDGMENTS

REFERENCES

Aguirre AJ, Meyers RM, Weir BA, Vazquez F, Zhang CZ, Ben-David U, Cook A, Ha G, Harrington WF, Doshi MB, et al. (2016). Genomic copy number dictates a gene-independent cell response to CRISPR/Cas9 targeting. Cancer Discov. 6, 914–929. [PubMed: 27260156]

Antonarakis ES, Heath EI, Posadas EM, Yu EY, Harrison MR, Bruce JY, Cho SY, Wilding GE, Fetterly GJ, Hangauer DG, et al. (2013). A phase 2 study of KX2-391, an oral inhibitor of Src kinase and tubulin polymerization, in men with bone-metastatic castration-resistant prostate cancer. Cancer Chemother. Pharmacol. 71, 883–892. [PubMed: 23314737]

Barrett A, Pellet-Many C, Zachary IC, Evans IM, and Frankel P (2013). p130Cas: a key signalling node in health and disease. Cell. Signal. 25, 766–777. [PubMed: 23277200]

Blake DR, Vaseva AV, Hodge RG, Kline MP, Gilbert TSK, Tyagi V, Huang D, Whiten GC, Larson JE, Wang X, et al. (2019). Application of a MYC degradation screen identifies sensitivity to CDK9 inhibitors in KRAS-mutant pancreatic cancer. Sci. Signal. 12, eaav7259. [PubMed: 31311847]

Blasco RB, Francoz S, Santamaría D, Cañamero M, Dubus P, Charron J, Baccarini M, and Barbacid M (2011). c-Raf, but not B-Raf, is essential for development of K-Ras oncogene-driven non-small cell lung carcinoma. Cancer Cell 19, 652–663. [PubMed: 21514245]

Boehmerle W, Zhang K, Sivula M, Heidrich FM, Lee Y, Jordt S-E, and Ehrlich BE (2007). Chronic exposure to paclitaxel diminishes phosphoinositide signaling by calpain-mediated neuronal calcium sensor-1 degradation. Proc. Natl. Acad. Sci. USA 104, 11103–11108. [PubMed: 17581879]

Boj SF, Hwang CI, Baker LA, Chio II, Engle DD, Corbo V, Jager M, Ponz-Sarvise M, Tiriac H, Spector MS, et al. (2015). Organoid models of human and mouse ductal pancreatic cancer. Cell 160, 324–338. [PubMed: 25557080]

Brenner JC, Graham MP, Kumar B, Saunders LM, Kupfer R, Lyons RH, Bradford CR, and Carey TE (2010). Genotyping of 73 UM-SCC head and neck squamous cell carcinoma cell lines. Head Neck 32, 417–426. [PubMed: 19760794]

Camacho Leal M.d.P., Sciortino M, Tornillo G, Colombo S, Defilippi P, and Cabodi S (2015). p130Cas/BCAR1 scaffold protein in tissue homeostasis and pathogenesis. Gene 562, 1–7. [PubMed: 25727852]

Campbell PM, Groehler AL, Lee KM, Ouellette MM, Khazak V, and Der CJ (2007). K-Ras promotes growth transformation and invasion of immortalized human pancreatic cells by Raf and phosphatidylinositol 3-kinase signaling. Cancer Res. 67, 2098–2106. [PubMed: 17332339]

Canon J, Rex K, Saiki AY, Mohr C, Cooke K, Bagal D, Gaida K, Holt T, Knutson CG, Koppada N, et al. (2019). The clinical KRAS(G12C) inhibitor AMG 510 drives anti-tumour immunity. Nature 575, 217–223. [PubMed: 31666701]

Childs EJ, Mocci E, Campa D, Bracci PM, Gallinger S, Goggins M, Li D, Neale RE, Olson SH, Scelo G, et al. (2015). Common variation at 2p13.3, 3q29, 7p13 and 17q25.1 associated with susceptibility to pancreatic cancer. Nat. Genet. 47, 911–916. [PubMed: 26098869]

Collins MA, Bednar F, Zhang Y, Brisset JC, Galbán S, Galbán CJ, Rakshit S, Flannagan KS, Adsay NV, and Pasca di Magliano M (2012). Oncogenic Kras is required for both the initiation and maintenance of pancreatic cancer in mice. J. Clin. Invest. 122, 639–653. [PubMed: 22232209]

Collisson EA, Trejo CL, Silva JM, Gu S, Korkola JE, Heiser LM, Charles RP, Rabinovich BA, Hann B, Dankort D, et al. (2012). A central role for RAF→MEK→ERK signaling in the genesis of pancreatic ductal adenocarcinoma. Cancer Discov. 2, 685–693. [PubMed: 22628411]

Conacci-Sorrell M, Ngouenet C, and Eisenman RN (2010). Myc-nick: a cytoplasmic cleavage product of Myc that promotes alpha-tubulin acetylation and cell differentiation. Cell 142, 480–493. [PubMed: 20691906]

Cox AD, Fesik SW, Kimmelman AC, Luo J, and Der CJ (2014). Drugging the undruggable RAS: Mission possible? Nat. Rev. Drug Discov. 13, 828–851. [PubMed: 25323927]

Dai Y, Yu C, Singh V, Tang L, Wang Z, McInistry R, Dent P, and Grant S (2001). Pharmacological inhibitors of the mitogen-activated protein kinase (MAPK) kinase/MAPK cascade interact synergistically with UCN-01 to induce mitochondrial dysfunction and apoptosis in human leukemia cells. Cancer Res. 61, 5106–5115. [PubMed: 11431348]

Dang CV (2012). MYC on the path to cancer. Cell 149, 22–35. [PubMed: 22464321]

Dang CV, Reddy EP, Shokat KM, and Soucek L (2017). Drugging the 'undruggable' cancer targets. Nat. Rev. Cancer 17, 502–508. [PubMed: 28643779]

Davis S, Charles PD, He L, Mowlds P, Kessler BM, and Fischer R (2017). Expanding proteome coverage with charge ordered parallel ion analysis (CHOPIN) combined with broad specificity proteolysis. J. Proteome Res. 16, 1288–1299. [PubMed: 28164708]

De Gendt K, Denolet E, Willems A, Daniels VW, Clinckemalie L, Denayer S, Wilkinson MF, Claessens F, Swinnen JV, and Verhoeven G (2011). Expression of Tubb3, a beta-tubulin isotype, is regulated by androgens in mouse and rat Sertoli cells. Biol. Reprod. 85, 934–945. [PubMed: 21734264]

Dingar D, Tu WB, Resetca D, Lourenco C, Tamachi A, De Melo J, Houlahan KE, Kalkat M, Chan PK, Boutros PC, et al. (2018). MYC dephosphorylation by the PP1/PNUTS phosphatase complex regulates chromatin binding and protein stability. Nat. Commun. 9, 3502. [PubMed: 30158517]

Downward J (2015). RAS synthetic lethal screens revisited: still seeking the elusive prize? Clin. Cancer Res. 21, 1802–1809. [PubMed: 25878361]

Duncan JS, Whittle MC, Nakamura K, Abell AN, Midland AA, Zawistowski JS, Johnson NL, Granger DA, Jordan NV, Darr DB, et al. (2012). Dynamic reprogramming of the kinome in response to targeted MEK inhibition in triple-negative breast cancer. Cell 149, 307–321. [PubMed: 22500798]

Farrell AS, and Sears RC (2014). MYC degradation. CSH Perspect. Med. 4, a014365.

Flaherty KT, Robert C, Hersey P, Nathan P, Garbe C, Milhem M, Demidov LV, Hassel JC, Rutkowski P, Mohr P, et al.; METRIC Study Group (2012). Improved survival with MEK inhibition in BRAF-mutated melanoma. N. Engl. J. Med. 367, 107–114. [PubMed: 22663011]

Foucquier J, and Guedj M (2015). Analysis of drug combinations: current methodological landscape. Pharmacol. Res. Perspect. 3, e00149. [PubMed: 26171228]

Hallin J, Engstrom LD, Hargis L, Calinisan A, Aranda R, Briere DM, Sudhakar N, Bowcut V, Baer BR, Ballard JA, et al. (2020). The KRAS(G12C) Inhibitor MRTX849 provides insight toward therapeutic susceptibility of KRAS-mutant cancers in mouse models and patients. Cancer Discov. 10, 54–71. [PubMed: 31658955]

Hantschel O, Rix U, and Superti-Furga G (2008). Target spectrum of the BCR-ABL inhibitors imatinib, nilotinib and dasatinib. Leuk. Lymphoma 49, 615–619. [PubMed: 18398720]

Hart T, and Moffat J (2016). BAGEL: a computational framework for identifying essential genes from pooled library screens. BMC Bioinformatics 17, 164. [PubMed: 27083490]

Hatzivassiliou G, Song K, Yen I, Brandhuber BJ, Anderson DJ, Alvarado R, Ludlam MJ, Stokoe D, Gloor SL, Vigers G, et al. (2010). RAF inhibitors prime wild-type RAF to activate the MAPK pathway and enhance growth. Nature 464, 431–435. [PubMed: 20130576]

Hayes TK, Neel NF, Hu C, Gautam P, Chenard M, Long B, Aziz M, Kassner M, Bryant KL, Pierobon M, et al. (2016). Long-term ERK inhibition in KRAS-mutant pancreatic cancer is associated with MYC degradation and senescence-like growth suppression. Cancer Cell 29, 75–89. [PubMed: 26725216]

He TC, Sparks AB, Rago C, Hermeking H, Zawel L, da Costa LT, Morin PJ, Vogelstein B, and Kinzler KW (1998). Identification of c-MYC as a target of the APC pathway. Science 281, 1509–1512. [PubMed: 9727977]

Hermeking H, Rago C, Schuhmacher M, Li Q, Barrett JF, Obaya AJ, O'Connell BC, Mateyak MK, Tam W, Kohlhuber F, et al. (2000). Identification of CDK4 as a target of c-MYC. Proc. Natl. Acad. Sci. USA 97, 2229–2234. [PubMed: 10688915]

Huang A, Garraway LA, Ashworth A, and Weber B (2020). Synthetic lethality as an engine for cancer drug target discovery. Nat. Rev. Drug Discov. 19, 23–38. [PubMed: 31712683]

Jones S, Zhang X, Parsons DW, Lin JC, Leary RJ, Angenendt P, Mankoo P, Carter H, Kamiyama H, Jimeno A, et al. (2008). Core signaling pathways in human pancreatic cancers revealed by global genomic analyses. Science 321, 1801–1806. [PubMed: 18772397]

Jouhilahti EM, Peltonen S, and Peltonen J (2008). Class III beta-tubulin is a component of the mitotic spindle in multiple cell types. J. Histochem. Cytochem. 56, 1113–1119. [PubMed: 18796406]

Karreth FA, Frese KK, DeNicola GM, Baccarini M, and Tuveson DA (2011). C-Raf is required for the initiation of lung cancer by K-Ras(G12D). Cancer Discov. 1, 128–136. [PubMed: 22043453]

Kim KB, Kefford R, Pavlick AC, Infante JR, Ribas A, Sosman JA, Fecher LA, Millward M, McArthur GA, Hwu P, et al. (2013). Phase II study of the MEK1/MEK2 inhibitor Trametinib in patients with metastatic BRAF-mutant cutaneous melanoma previously treated with or without a BRAF inhibitor. J. Clin. Oncol. 31, 482–489. [PubMed: 23248257]

Kiyokawa E, Hashimoto Y, Kobayashi S, Sugimura H, Kurata T, and Matsuda M (1998). Activation of Rac1 by a Crk SH3-binding protein, DOCK180. Genes Dev. 12, 3331–3336. [PubMed: 9808620]

König R, Chiang CY, Tu BP, Yan SF, DeJesus PD, Romero A, Bergauer T, Orth A, Krueger U, Zhou Y, and Chanda SK (2007). A probability-based approach for the analysis of large-scale RNAi screens. Nat. Methods 4, 847–849. [PubMed: 17828270]

Kotecha N, Krutzik PO, and Irish JM (2010). Web-based analysis and publication of flow cytometry experiments. Curr. Protoc. Cytom. Chapter 10, Unit10.17.

Krämer A, Green J, Pollard J Jr., and Tugendreich S (2014). Causal analysis approaches in Ingenuity Pathway Analysis. Bioinformatics 30, 523–530. [PubMed: 24336805]

Lee KM, Cao D, Itami A, Pour PM, Hruban RH, Maitra A, and Ouellette MM (2007). Class III β-tubulin, a marker of resistance to paclitaxel, is overexpressed in pancreatic ductal adenocarcinoma and intraepithelial neoplasia. Histopathology 51, 539–546. [PubMed: 17714470]

Lenoir WF, Lim TL, and Hart T (2018). PICKLES: the database of pooled in-vitro CRISPR knockout library essentiality screens. Nucleic Acids Res. 46 (D1), D776–D780. [PubMed: 29077937]

Little AS, Balmanno K, Sale MJ, Newman S, Dry JR, Hampson M, Edwards PA, Smith PD, and Cook SJ (2011). Amplification of the driving oncogene, KRAS or BRAF, underpins acquired resistance to MEK1/2 inhibitors in colorectal cancer cells. Sci. Signal. 4, ra17. [PubMed: 21447798]

Liu T, Hu W, Dalton HJ, Choi HJ, Huang J, Kang Y, Pradeep S, Miyake T, Song JH, Wen Y, et al. (2013). Targeting SRC and tubulin in mucinous ovarian carcinoma. Clin. Cancer Res. 19, 6532–6543. [PubMed: 24100628]

MacKeigan JP, Collins TS, and Ting JP (2000). MEK inhibition enhances paclitaxel-induced tumor apoptosis. J. Biol. Chem. 275, 38953–38956. [PubMed: 11038347]

Martz CA, Ottina KA, Singleton KR, Jasper JS, Wardell SE, Peraza-Penton A, Anderson GR, Winter PS, Wang T, Alley HM, et al. (2014). Systematic identification of signaling pathways with potential to confer anti-cancer drug resistance. Sci. Signal. 7, ra121. [PubMed: 25538079]

McCarroll JA, Sharbeen G, Liu J, Youkhana J, Goldstein D, McCarthy N, Limbri LF, Dischl D, Ceyhan GO, Erkan M, et al. (2015). βIII-tubulin: a novel mediator of chemoresistance and metastases in pancreatic cancer. Oncotarget 6, 2235–2249. [PubMed: 25544769]

McCormick F (2015). KRAS as a therapeutic target. Clin. Cancer Res. 21, 1797–1801. [PubMed: 25878360]

McDaid HM, and Horwitz SB (2001). Selective potentiation of paclitaxel (taxol)-induced cell death by mitogen-activated protein kinase kinase inhibition in human cancer cell lines. Mol. Pharmacol. 60, 290–301. [PubMed: 11455016]

McFarland JM, Ho ZV, Kugener G, Dempster JM, Montgomery PG, Bryan JG, Krill-Burger JM, Green TM, Vazquez F, Boehm JS, et al. (2018). Improved estimation of cancer dependencies from large-scale RNAi screens using model-based normalization and data integration. Nat. Commun. 9, 4610. [PubMed: 30389920]

Meyers RM, Bryan JG, McFarland JM, Weir BA, Sizemore AE, Xu H, Dharia NV, Montgomery PG, Cowley GS, Pantel S, et al. (2017). Computational correction of copy number effect improves specificity of CRISPR-Cas9 essentiality screens in cancer cells. Nat. Genet. 49, 1779–1784. [PubMed: 29083409]

Morris EJ, Jha S, Restaino CR, Dayananth P, Zhu H, Cooper A, Carr D, Deng Y, Jin W, Black S, et al. (2013). Discovery of a novel ERK inhibitor with activity in models of acquired resistance to BRAF and MEK inhibitors. Cancer Discov. 3, 742–750. [PubMed: 23614898]

Naing A, Cohen R, Dy GK, Hong DS, Dyster L, Hangauer DG, Kwan R, Fetterly G, Kurzrock R, and Adjei AA (2013). A phase I trial of KX2-391, a novel non-ATP competitive substrate-pocket-directed SRC inhibitor, in patients with advanced malignancies. Invest. New Drugs 31, 967–973. [PubMed: 23361621]

Nikonova AS, Gaponova AV, Kudinov AE, and Golemis EA (2014). CAS proteins in health and disease: an update. IUBMB Life 66, 387–395. [PubMed: 24962474]

Niu L, Yang J, Yan W, Yu Y, Zheng Y, Ye H, Chen Q, and Chen L (2019). Reversible binding of the anticancer drug KXO1 (tirbanibulin) to the colchicine-binding site of β-tubulin explains KXO1's low clinical toxicity. J. Biol. Chem. 294, 18099–18108. [PubMed: 31628188]

Okano J, and Rustgi AK (2001). Paclitaxel induces prolonged activation of the Ras/MEK/ERK pathway independently of activating the programmed cell death machinery. J. Biol. Chem. 276, 19555–19564. [PubMed: 11278851]

Orr GA, Verdier-Pinard P, McDaid H, and Horwitz SB (2003). Mechanisms of Taxol resistance related to microtubules. Oncogene 22, 7280–7295. [PubMed: 14576838]

Ozkan-Dagliyan I, Diehl JN, George SD, Schaefer A, Papke B, Klotz-Noack K, Waters AM, Goodwin CM, Gautam P, Pierobon M, et al. (2020). Low-dose vertical inhibition of the RAF-MEK-ERK cascade causes apoptotic death of KRAS-mutant cancers. Cell Rep. 31, 107764. [PubMed: 32553168]

Papke B, and Der CJ (2017). Drugging RAS: Know the enemy. Science 355, 1158–1163. [PubMed: 28302824]

Perez EA (2009). Microtubule inhibitors: Differentiating tubulin-inhibiting agents based on mechanisms of action, clinical activity, and resistance. Mol. Cancer Ther. 8, 2086–2095. [PubMed: 19671735]

Poulikakos PI, Zhang C, Bollag G, Shokat KM, and Rosen N (2010). RAF inhibitors transactivate RAF dimers and ERK signalling in cells with wild-type BRAF. Nature 464, 427–430. [PubMed: 20179705]

Prior IA, Hood FE, and Hartley JL (2020). The frequency of RAS mutations in cancer. Cancer Res. 80, 2969–2974. [PubMed: 32209560]

R Core Team (2013). R: A language and environment for statistical computing (Vienna, Austria: R Foundation for Statistical Computing).

Reynolds AB, Kanner SB, Bouton AH, Schaller MD, Weed SA, Flynn DC, and Parsons JT (2014). SRChing for the substrates of Src. Oncogene 33, 4537–4547. [PubMed: 24121272]

Ryan MB, and Corcoran RB (2018). Therapeutic strategies to target RAS-mutant cancers. Nat. Rev. Clin. Oncol. 15, 709–720. [PubMed: 30275515]

Ryan MB, Fece de la Cruz F, Phat S, Myers DT, Wong E, Shahzade HA, Hong CB, and Corcoran RB (2020). Vertical pathway inhibition overcomes adaptive feedback resistance to KRAS(G12C) inhibition. Clin. Cancer Res. 26, 1633–1643. [PubMed: 31776128]

Schmid-Alliana A, Menou L, Manié S, Schmid-Antomarchi H, Millet MA, Giuriato S, Ferrua B, and Rossi B (1998). Microtubule integrity regulates src-like and extracellular signal-regulated kinase activities in human promonocytic cells. Importance for interleukin-1 production. J. Biol. Chem. 273, 3394–3400. [PubMed: 9452460]

Schneider CA, Rasband WS, and Eliceiri KW (2012). NIH Image to ImageJ: 25 years of image analysis. Nat. Methods 9, 671–675. [PubMed: 22930834]

Shinohara-Gotoh Y, Nishida E, Hoshi M, and Sakai H (1991). Activation of microtubule-associated protein kinase by microtubule disruption in quiescent rat 3Y1 cells. Exp. Cell Res. 193, 161–166. [PubMed: 1847331]

Siegel RL, Miller KD, and Jemal A (2020). Cancer statistics, 2020. CA Cancer J. Clin. 70, 7–30. [PubMed: 31912902]

Smith HW, Marra P, and Marshall CJ (2008). uPAR promotes formation of the p130Cas-Crk complex to activate Rac through DOCK180. J. Cell Biol. 182, 777–790. [PubMed: 18725541]

Smolinski MP, Bu Y, Clements J, Gelman IH, Hegab T, Cutler DL, Fang JWS, Fetterly G, Kwan R, Barnett A, et al. (2018). Discovery of novel dual mechanism of action Src signaling and tubulin polymerization inhibitors (KX2-391 and KX2-361). J. Med. Chem. 61, 4704–4719. [PubMed: 29617135]

Soucek L, Whitfield J, Martins CP, Finch AJ, Murphy DJ, Sodir NM, Karnezis AN, Swigart LB, Nasi S, and Evan GI (2008). Modelling Myc inhibition as a cancer therapy. Nature 455, 679–683. [PubMed: 18716624]

Soucek L, Whitfield JR, Sodir NM, Massó-Vallés D, Serrano E, Karnezis AN, Swigart LB, and Evan GI (2013). Inhibition of Myc family proteins eradicates KRas-driven lung cancer in mice. Genes Dev. 27, 504–513. [PubMed: 23475959]

Szklarczyk D, Franceschini A, Wyder S, Forslund K, Heller D, Huerta-Cepas J, Simonovic M, Roth A, Santos A, Tsafou KP, et al. (2015). STRING v10: protein-protein interaction networks, integrated over the tree of life. Nucleic Acids Res. 43, D447–D452. [PubMed: 25352553]

Tiriac H, Belleau P, Engle DD, Plenker D, Deschênes A, Somerville TDD, Froeling FEM, Burkhart RA, Denroche RE, Jang GH, et al. (2018). Organoid profiling identifies common responders to chemotherapy in pancreatic cancer. Cancer Discov. 8, 1112–1129. [PubMed: 29853643]

Tsherniak A, Vazquez F, Montgomery PG, Weir BA, Kryukov G, Cowley GS, Gill S, Harrington WF, Pantel S, Krill-Burger JM, et al. (2017). Defining a cancer dependency map. Cell 170, 564–576.e16. [PubMed: 28753430]

Tu C, Li J, Bu Y, Hangauer D, and Qu J (2012). An ion-current-based, comprehensive and reproducible proteomic strategy for comparative characterization of the cellular responses to novel anti-cancer agents in a prostate cell model. J. Proteomics 77, 187–201. [PubMed: 22982362]

Vallejo A, Perurena N, Guruceaga E, Mazur PK, Martinez-Canarias S, Zandueta C, Valencia K, Arricibita A, Gwinn D, Sayles LC, et al. (2017). An integrative approach unveils FOSL1 as an oncogene vulnerability in KRAS-driven lung and pancreatic cancer. Nat. Commun. 8, 14294. [PubMed: 28220783]

Vaseva AV, Blake DR, Gilbert TSK, Ng S, Hostetter G, Azam SH, Ozkan-Dagliyan I, Gautam P, Bryant KL, Pearce KH, et al. (2018). KRAS suppression-induced degradation of MYC is antagonized by a MEK5-ERK5 compensatory mechanism. Cancer Cell 34, 807–822.e7. [PubMed: 30423298]

Wang T, Yu H, Hughes NW, Liu B, Kendirli A, Klein K, Chen WW, Lander ES, and Sabatini DM (2017). Gene essentiality profiling reveals gene networks and synthetic lethal interactions with oncogenic Ras. Cell 168, 890–903.e15. [PubMed: 28162770]

Waters AM, and Der CJ (2018). KRAS: the critical driver and therapeutic target for pancreatic cancer. Cold Spring Harb. Perspect. Med. 8, a031435. [PubMed: 29229669]

Wolpin BM, Rizzato C, Kraft P, Kooperberg C, Petersen GM, Wang Z, Arslan AA, Beane-Freeman L, Bracci PM, Buring J, et al. (2014). Genome-wide association study identifies multiple susceptibility loci for pancreatic cancer. Nat. Genet. 46, 994–1000. [PubMed: 25086665]

Wu X, Tu X, Joeng KS, Hilton MJ, Williams DA, and Long F (2008). Rac1 activation controls nuclear localization of beta-catenin during canonical Wnt signaling. Cell 133, 340–353. [PubMed: 18423204]

Xue JY, Zhao Y, Aronowitz J, Mai TT, Vides A, Qeriqi B, Kim D, Li C, de Stanchina E, Mazutis L, et al. (2020). Rapid non-uniform adaptation to conformation-specific KRAS(G12C) inhibition. Nature 577, 421–425. [PubMed: 31915379]

Yen I, Shanahan F, Merchant M, Orr C, Hunsaker T, Durk M, La H, Zhang X, Martin SE, Lin E, et al. (2018). Pharmacological induction of RAS-GTP confers RAF inhibitor sensitivity in KRAS mutant tumors. Cancer Cell 34, 611–625.e7. [PubMed: 30300582]

Ying H, Kimmelman AC, Lyssiotis CA, Hua S, Chu GC, Fletcher-Sananikone E, Locasale JW, Son J, Zhang H, Coloff JL, et al. (2012). Oncogenic Kras maintains pancreatic tumors through regulation of anabolic glucose metabolism. Cell 149, 656–670. [PubMed: 22541435]

Yochum GS, Cleland R, and Goodman RH (2008). A genome-wide screen for beta-catenin binding sites identifies a downstream enhancer element that controls c-Myc gene expression. Mol. Cell. Biol. 28, 7368–7379. [PubMed: 18852287]

Zhang JH, Chung TD, and Oldenburg KR (1999). A simple statistical parameter for use in evaluation and validation of high throughput screening Assays. J. Biomol. Screen. 4, 67–73. [PubMed: 10838414]

Zhong J, Jermusyk A, Wu L, Hoskins JW, Collins I, Mocci E, Zhang M, Song L, Chung CC, Zhang T, et al. (2020). A Transcriptome-Wide Association Study Identifies Novel Candidate Susceptibility Genes for Pancreatic Cancer. J. Natl. Cancer Inst. 112, 1003–1012. [PubMed: 31917448]

Highlights

- p130Cas and βIII-tubulin support PDAC growth by enhancing MYC expression

- p130Cas transcriptionally regulates MYC through SRC-p130Cas-DOCK1-RAC1-β-catenin

- Microtubules post-translationally regulate MYC stability through calpains

- Triple targeting of ERK/p130Cas/tubulin with ERKi and KX2-391 inhibits PDAC growth
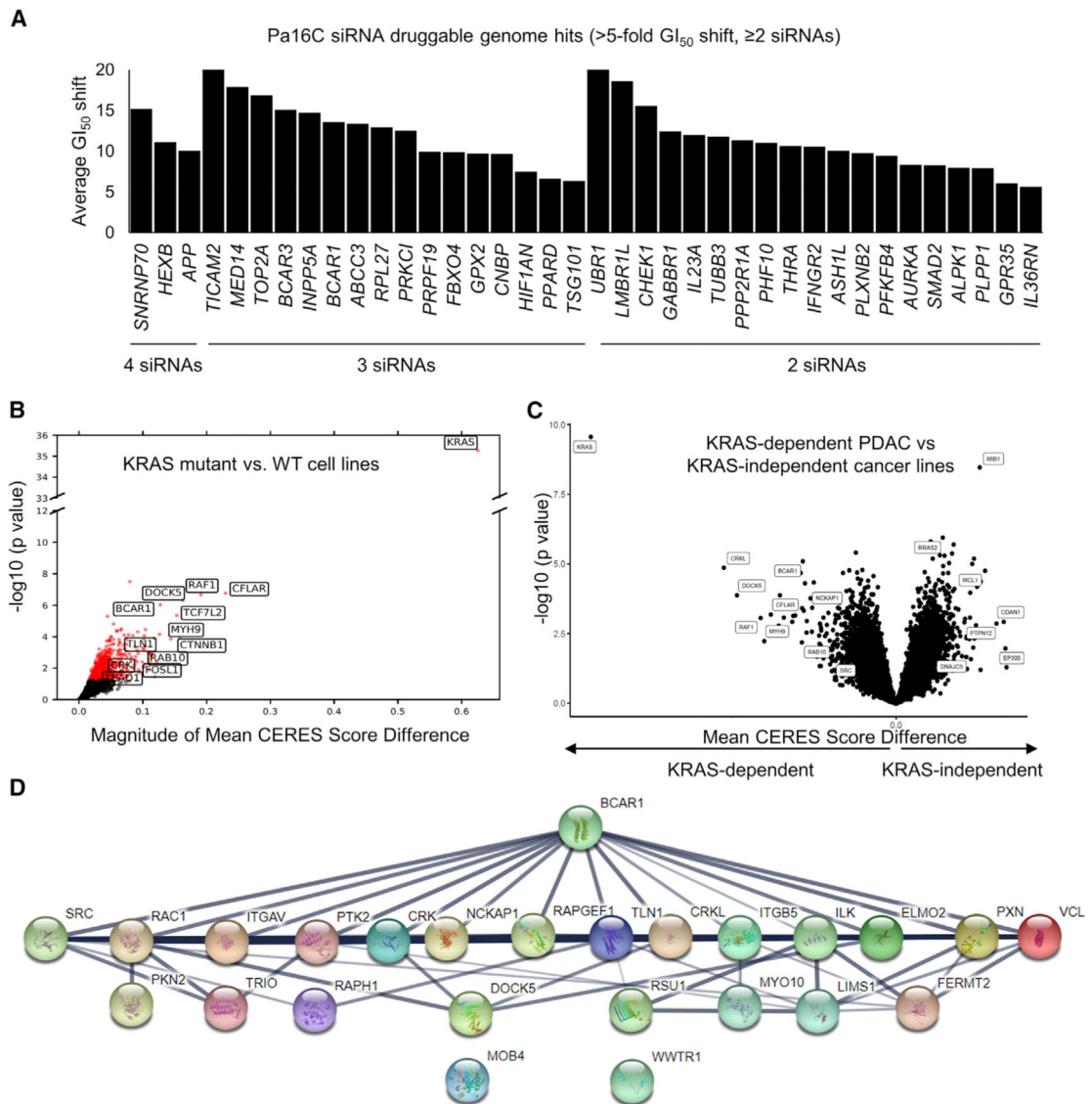
**Figure 1. Identification of genes that modulate ERK inhibitor sensitivity and synthetic lethality with mutant KRAS**

(A) Average ranking of the top 38 hits, stratified by the number of siRNAs that shifted the GI_{50} >5-fold compared to the controls and the average hit strength.

(B) Sensitizing genes from a CRISPR screen enriched in *KRAS* mutant cancers are shown in red ($p < 0.05$).

(C) Gene dependencies in *KRAS* mutant PDAC compared to *KRAS*-independent cancer cell lines.

(D) The top 25 correlated genes with *BCAR1* from a Pearson correlation were plotted using String.

See also Figure S1 and Tables S1 and S2.
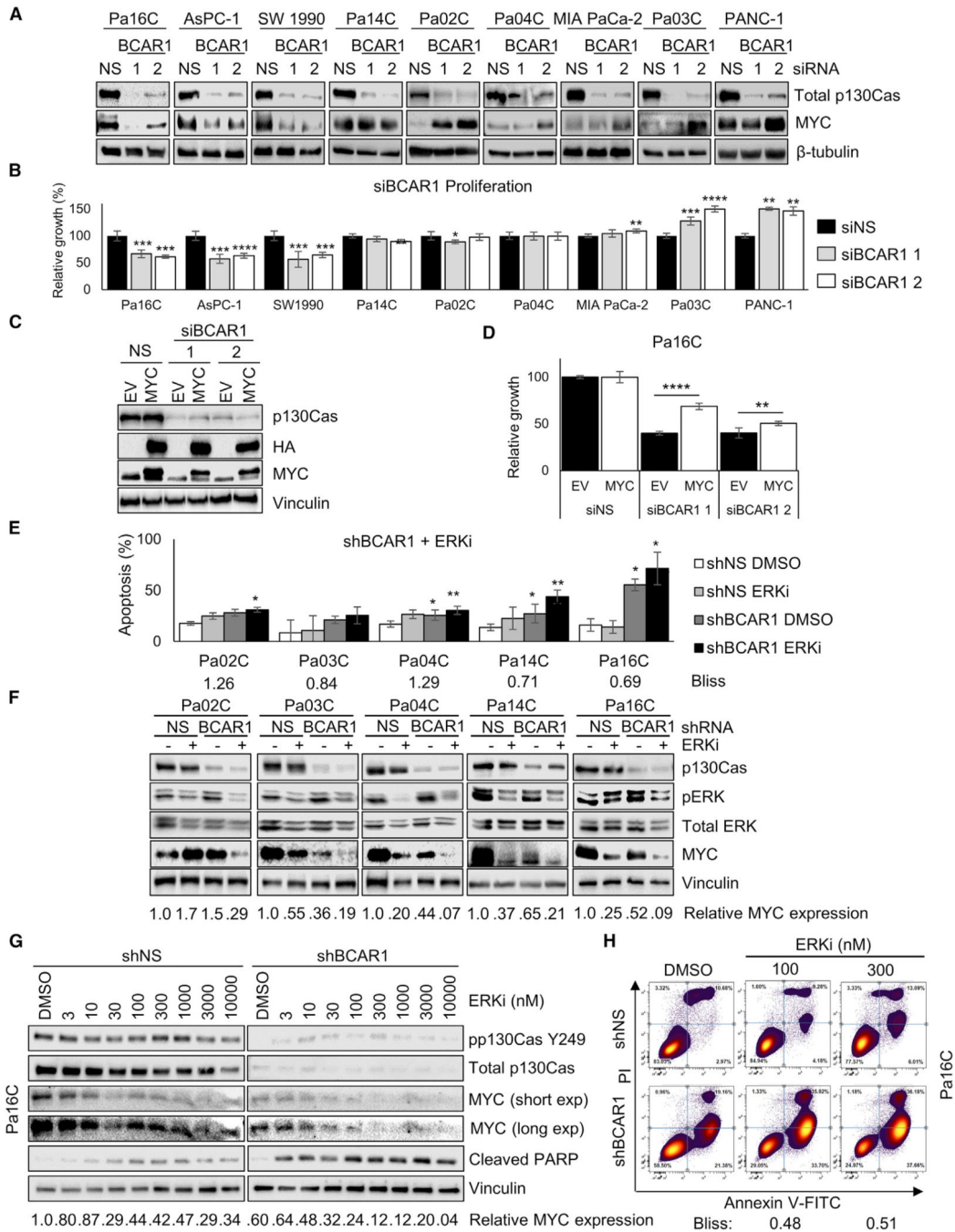
Figure 2. p130Cas suppression transcriptionally downregulates MYC and synergizes with ERKi
(A) Cells were treated with control siRNAs (siNS) or siRNAs targeting *BCAR1* (siBCAR1)
to assess MYC protein levels.

(B) Proliferation assays were performed on PDAC lines treated with siNS or siBCAR1 for
72 h. Data shown are normalized to siNS.

(C) Empty vector (EV) control or MYC-rescued Pa16C cells were treated with siNS or
siBCAR1 and p130Cas and MYC levels were assessed.

(D) Proliferation assays were performed on EV or MYC-rescued Pa16C cells treated with siNS or siBCAR1. Data shown are normalized to siNS.

(E) Apoptosis assays were performed on cells treated with shNS or shBCAR1 in the presence or absence of ERKi for 48 h.

(F) ERKi was added to cell lines treated with shNS or shBCAR1, and MYC levels were assessed.

(G) Pa16C cells stably expressing shNS or shBCAR1 were treated with ERKi, and p130Cas, MYC, and cleaved PARP levels were assessed.

(H) Pa16C cells expressing shNS or shBCAR1 were treated with ERKi, and apoptosis assays were performed.

Data in all panels are representative of three independent experiments and represented as mean ± SD. * = p value < 0.05, ** = p value < 0.01, *** = p value < 0.001, **** = p value < 0.0001. See also Figures S2–S4.
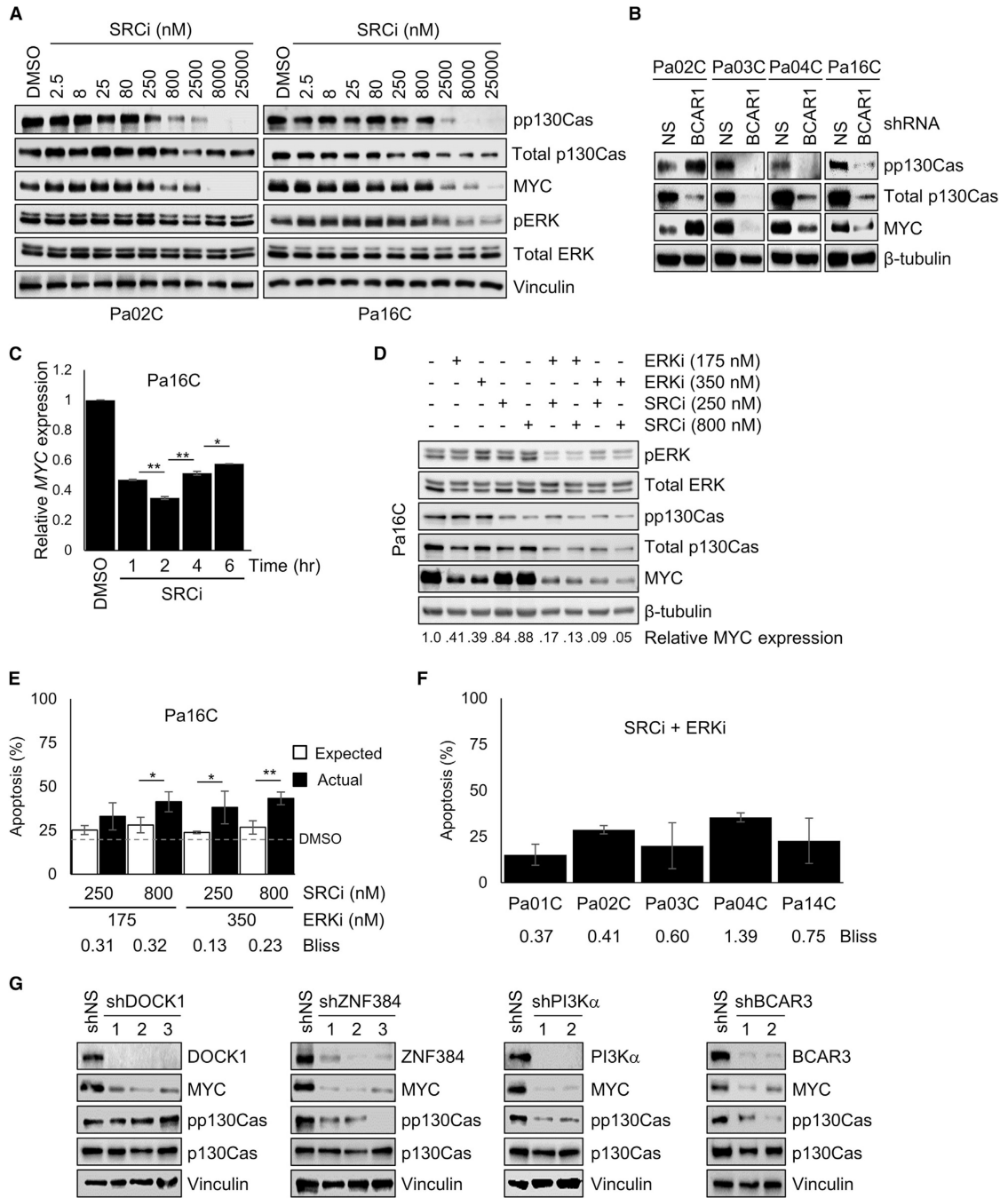
Figure 3. SRCi transcriptionally reduces MYC and causes apoptosis when combined with ERKi

(A) Cell lines were treated with SRCi for 48 h, and pp130Cas, MYC, and pERK protein levels were assessed.

(B) PDAC cell lines were infected with shNS or shBCAR1 and pp130Cas and MYC protein levels were assessed.

(C) *MYC* mRNA levels were assessed after treatment with 800 nM SRCi for the indicated times. Data are representative of two independent experiments and presented as mean ± SD.
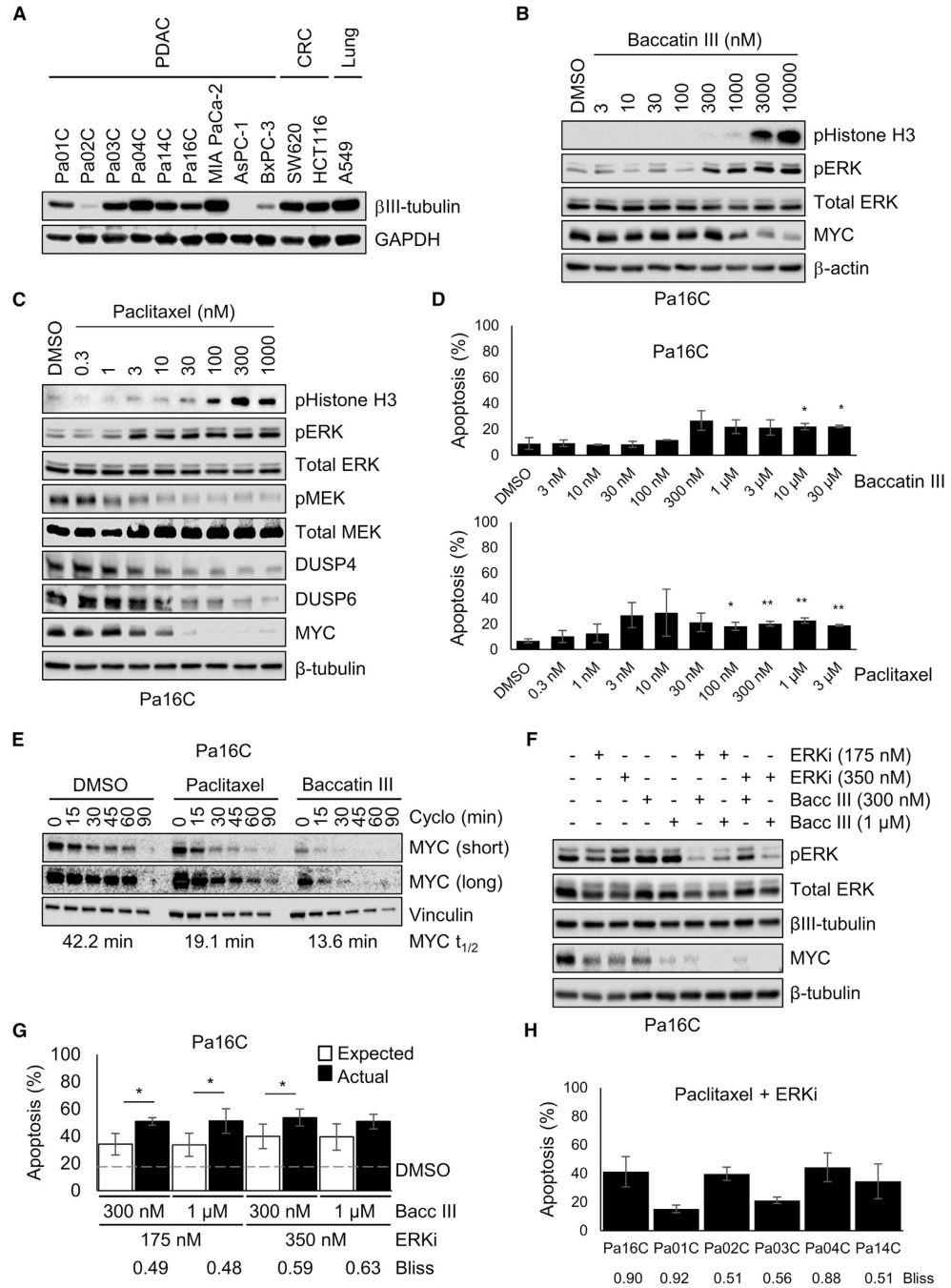
(D) Pa16C cells were treated with ERKi and/or SRCi for 72 h, and pERK, pp130Cas, and MYC levels were assessed.

(E) Pa16C cells were treated with ERKi and/or SRCi for 72 h, and apoptosis was assessed. "Expected" indicates the presumptive additive effect from the single-agent treatments. "Actual" indicates the observed combination effect. Data are averaged from three independent experiments and presented as mean ± SD.

(F) Cells were treated with SRCi and/or ERKi for 72 h, and apoptosis assays were performed. Data are averaged from three independent experiments and presented as mean ± SD.

(G) Pa16C cells were treated with shRNAs and pp130Cas, and MYC levels were assessed. Unless otherwise noted, data panels are representative of three independent experiments. * = p value < 0.05, ** = p value < 0.01. See also Figures S5 and S6.

Figure 4. Tubulin destabilizers reduce MYC protein half-life and cause apoptosis when combined with ERKi

(A) βIII-Tubulin protein levels were assessed in a panel of PDAC and other *KRAS* mutant cancer cell lines.

(B) Pa16C cells were treated with baccatin III for 48 h to assess MYC, pHistone H3 (S10), and pERK levels.

(C) Pa16C cells were treated with paclitaxel for 48 h to assess pHistone H3, pERK, pMEK, DUSP4/6, and MYC levels.

(D) Pa16C cells were treated with baccatin III or paclitaxel for 48 h, and apoptosis was assessed. Data are averaged from two independent experiments and presented as mean ± SD.
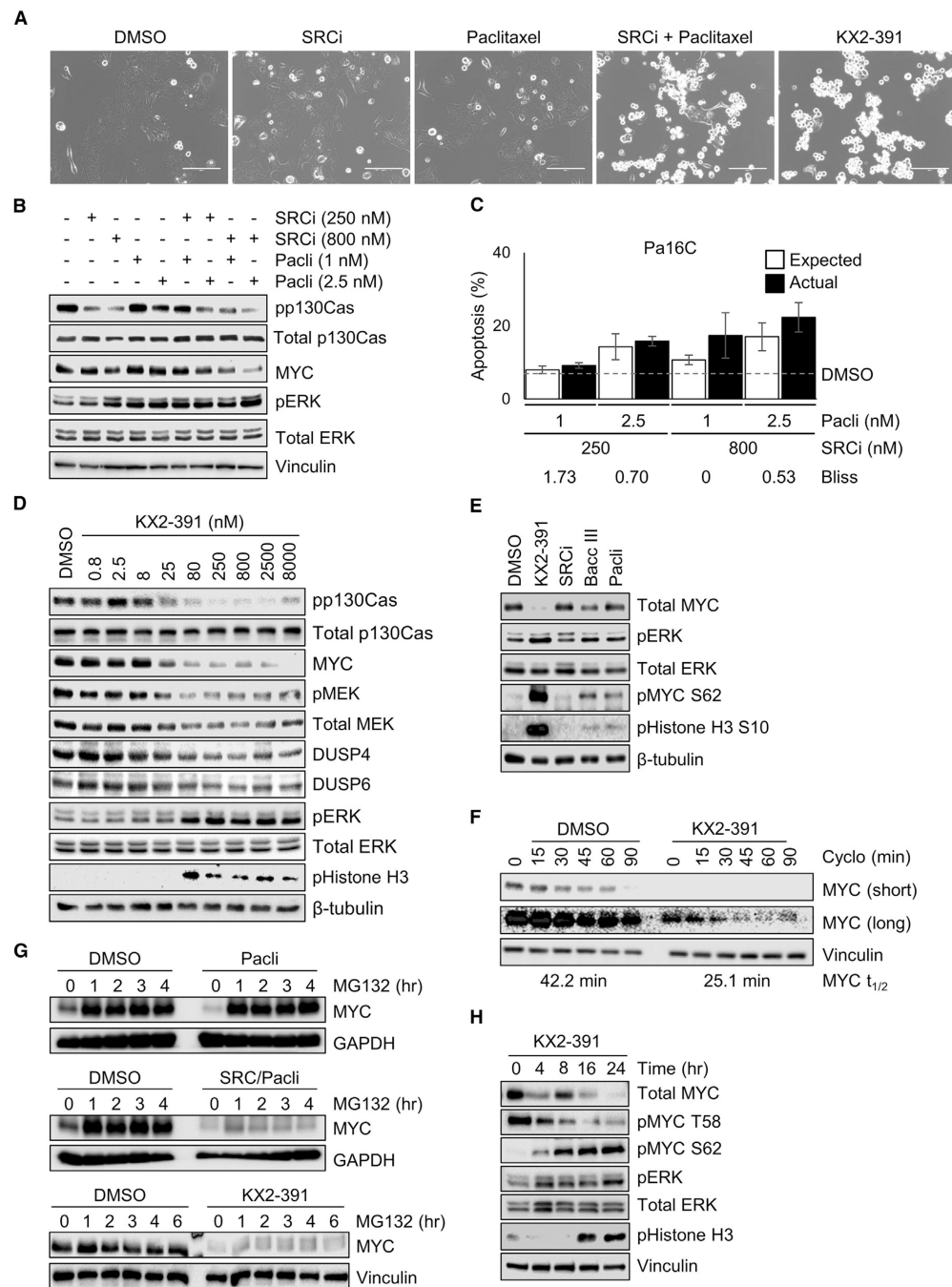
(E) Pa16C cells were treated with DMSO, paclitaxel, or baccatin III for 20 h before adding cycloheximide (cyclo) for the indicated times, and MYC protein half-life was determined by immunoblotting.

(F) Pa16C cells were treated with ERKi and/or baccatin III (Bacc III) for 72 h, and pERK and MYC levels were assessed.

(G) Pa16C cells were treated with ERKi and/or baccatin III for 72 h before assessing apoptosis.

(H) Cells were treated with paclitaxel and/or ERKi for 72 h, and apoptosis assays were performed. Unless otherwise noted, data panels are averaged from three independent experiments and presented as mean ± SD. * = p value < 0.05, ** = p value < 0.01.

See also Figures S7–S9 and Table S3.

Figure 5. KX2-391 phenocopies SRCi + and β-tubulin inhibition and potently suppresses MYC expression

(A) After 20-h treatment with the indicated inhibitors, cells were imaged. Scale bars, 200 μm.

(B) Cells were treated with SRCi and/or paclitaxel (Pacli) for 48 h, and pp130Cas, pERK, and MYC levels were assessed.

(C) Cells were treated with SRCi and/or Pacli for 48 h, and apoptosis was assessed. Data are averaged from three independent experiments and represented as mean ± SD.

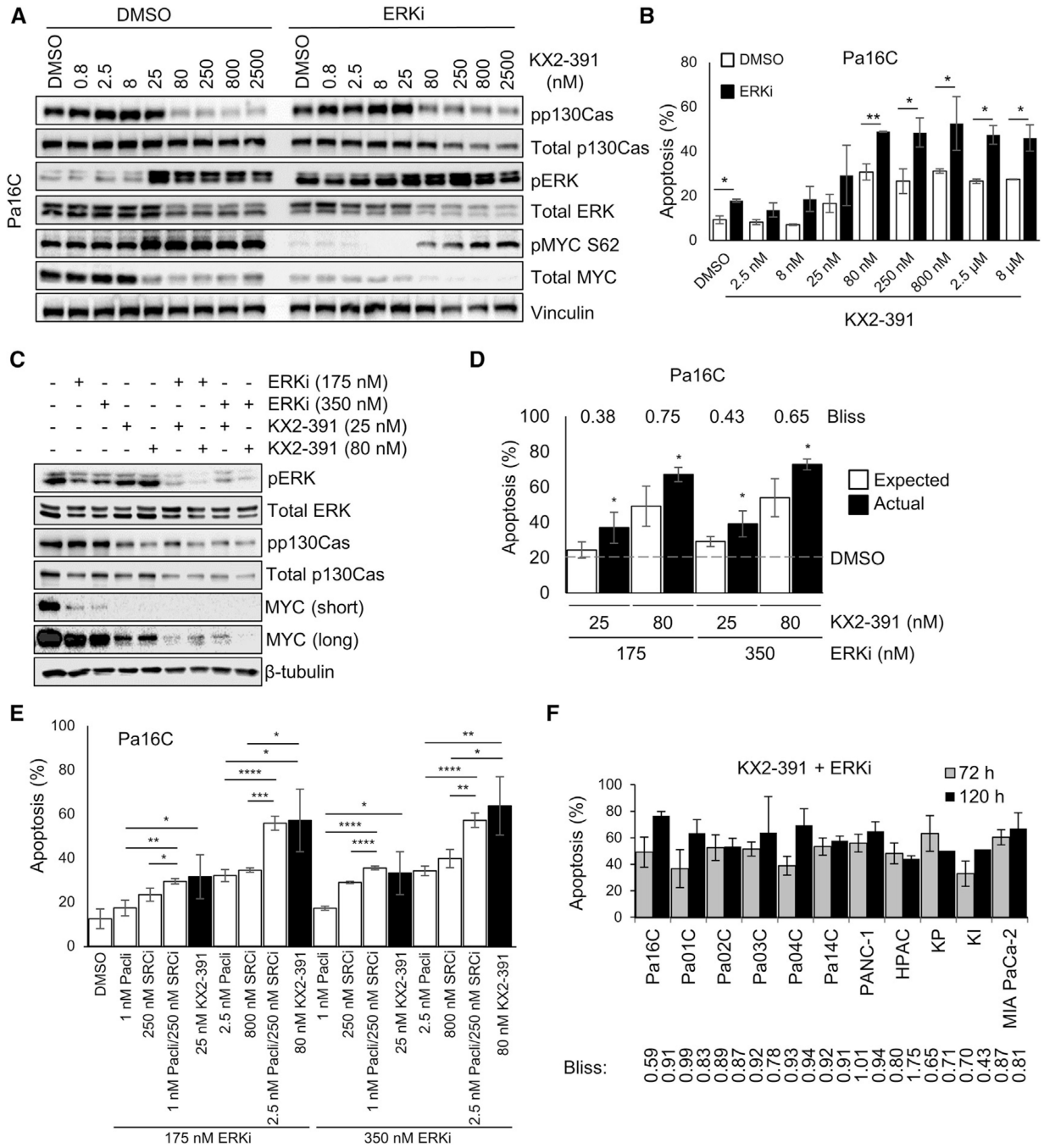(D) Cells were treated with KX2-391 for 48 h, and the indicated proteins were assessed.

(E) Cells were treated with the indicated compounds, and pHistone H3, ERK, and MYC abundance/phosphorylation was assessed.

(F) Cells were treated with DMSO or KX2-391 for 20 h before cycloheximide was added for the indicated times, and MYC protein half-life was determined.

(G) Cells were treated with the indicated inhibitors for 20 h before MG132 was added for the indicated times, and MYC accumulation was assessed.

(H) Cells were treated with KX2-391 (80 nM) for the indicated times to assess temporal changes to MYC abundance and phosphorylation.

Unless otherwise noted, data are representative of three independent experiments and represented as mean ± SD. See also Figure S9.

Figure 6. KX2-391 + ERKi combinations drive robust synergistic apoptosis

(A) Pa16C cells were treated with KX2-391 with DMSO or 350 nM ERKi for 72 h, and pERK and pMYC S62 protein levels were assessed. Data are representative of three independent experiments.

(B) Pa16C cells were treated as in (A), and apoptosis was assessed. Data are averaged from two independent experiments and are presented as mean ± SD.
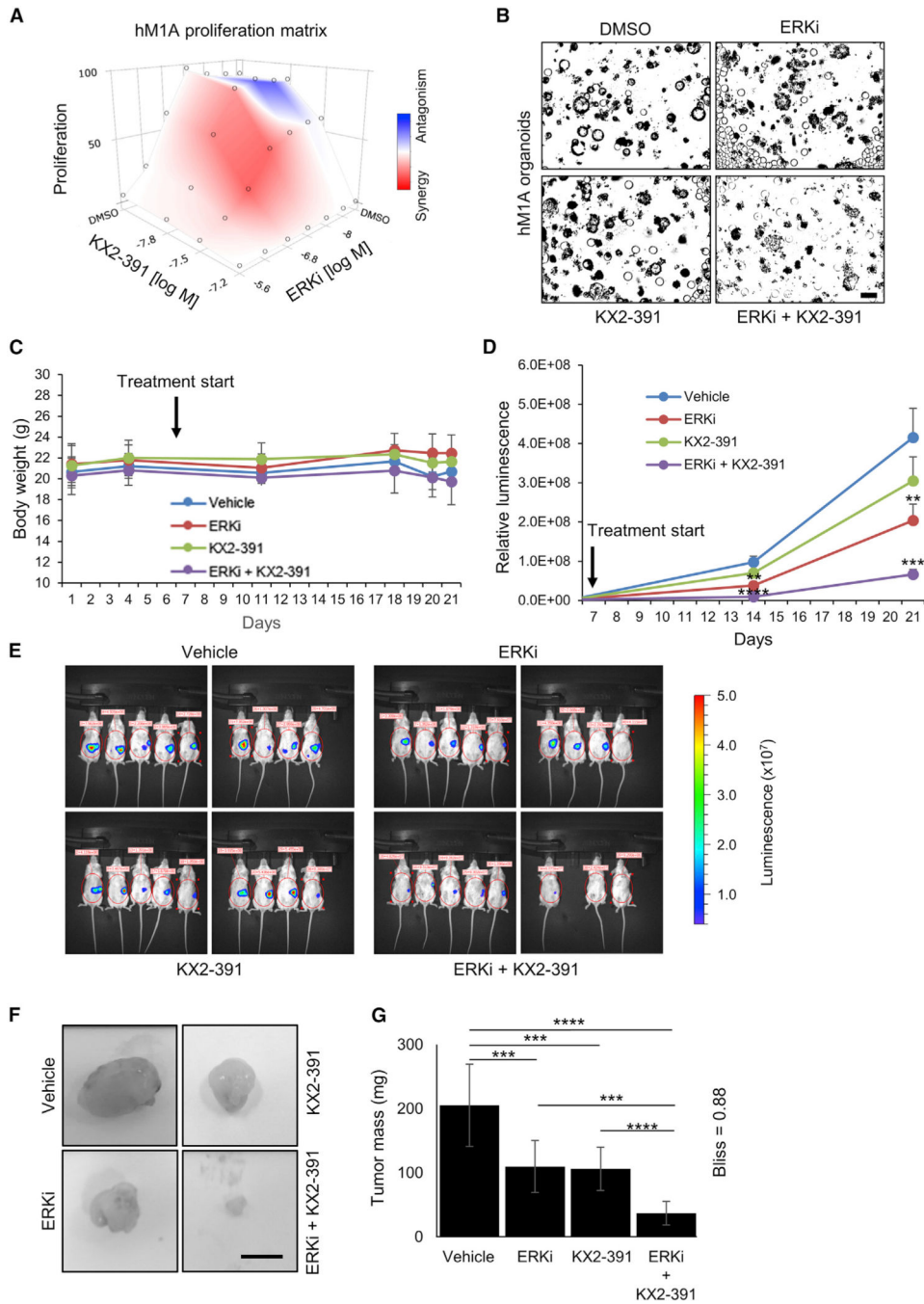
(C) Pa16C cells were treated with ERKi and/or KX2-391 for 72 h, and pERK, pp130Cas, and MYC protein levels were assessed. Data are representative of three independent experiments.

(D) Pa16C cells were treated as in (C), and apoptosis was assessed. Data are averaged from three independent experiments and presented as mean ± SD.

(E) Pa16C cells were treated with double or triple combinations as indicated for 72 h, and apoptosis was assessed. Data are averaged from three independent experiments and presented as mean ± SD.

(F) PDAC cell lines were treated with KX2-391 and ERKi for 72 h, and apoptosis was assessed. Data are averaged from three independent experiments and presented as mean ± SD. * = p value < 0.05, ** = p value < 0.01, *** = p value < 0.001, **** = p value < 0.0001. See also Figure S9.

Figure 7. KX2-391 + ERKi combinations inhibit growth in human PDAC organoids and a syngeneic, orthotopic mouse model of pancreatic cancer

(A) Patient-derived *KRAS* mutant PDAC organoids were treated with ERKi and/or KX2-391 for 7 days, and proliferation assays were performed. Data are averaged from three independent experiments.

(B) Organoids from (A) were imaged. Data are representative of three independent experiments. Scale bar, 200 μm.

(C) Mice were treated with vehicle, ERKi, KX2-391, or both, and body weight was monitored throughout the course of treatment.

(D) Luminescence of pancreatic tumors in mice from (C) was measured after 7 and 14 days of treatment. Data from each treatment group were averaged and are presented as mean ± SEM.

(E) Tumor-bearing mice from (C) and (D) were imaged at the end of the study. Data are presented as mean ± SEM.

(F) Representative tumors excised from the pancreas of mice in (E) were photographed. Scale bar, 0.5 cm.

(G) Tumors excised from each mouse in (E) were weighed and the data averaged within each treatment group. Data are represented as mean ± SD. * = p value < 0.05, ** = p value < 0.01, *** = p value < 0.001, **** = p value < 0.0001.

See also Figure S10 and Table S4.